

# Timing stability of millisecond pulsars and prospects for gravitational-wave detection

J. P. W. Verbiest,<sup>1,2,3\*</sup> M. Bailes,<sup>1</sup> W. A. Coles,<sup>4</sup> G. B. Hobbs,<sup>2</sup> W. van Straten,<sup>1</sup>  
D. J. Champion,<sup>2</sup> F. A. Jenet,<sup>5</sup> R. N. Manchester,<sup>2</sup> N. D. R. Bhat,<sup>1</sup>  
J. M. Sarkissian,<sup>2</sup> D. Yardley,<sup>2,6</sup> S. Burke-Spolaor,<sup>1,2</sup> A. W. Hotan<sup>7</sup> and X. P. You<sup>8</sup>

<sup>1</sup>*Swinburne University of Technology, Centre for Astrophysics and Supercomputing Mail #H39 P. O. Box 218 VIC 3122 Australia*

<sup>2</sup>*Australia Telescope National Facility – CSIRO P.O. Box 76, Epping, NSW, 1710 Australia*

<sup>3</sup>*Department of Physics, West Virginia University, P.O. Box 6315, WV 26506, USA*

<sup>4</sup>*Electrical and Computer Engineering, University of California at San Diego, La Jolla, CA 92093, USA*

<sup>5</sup>*CGWA, University of Texas at Brownsville, TX 78520, USA*

<sup>6</sup>*Sydney Institute for Astronomy, School of Physics A29, The University of Sydney, NSW 2006, Australia*

<sup>7</sup>*Curtin Institute for Radio Astronomy, Curtin University of Technology, Bentley, WA 6102, Australia*

<sup>8</sup>*School of Physical Science and Technology, Southwest University, 2 Tiansheng Road, Chongqing 400715, China*

Submitted 2009 Jun 19

## ABSTRACT

Analysis of high-precision timing observations of an array of  $\sim 20$  millisecond pulsars (a so-called “timing array”) may ultimately result in the detection of a stochastic gravitational-wave background. The feasibility of such a detection and the required duration of this type of experiment are determined by the achievable rms of the timing residuals and the timing stability of the pulsars involved. We present results of the first long-term, high-precision timing campaign on a large sample of millisecond pulsars used in gravitational-wave detection projects. We show that the timing residuals of most pulsars in our sample do not contain significant low-frequency noise that could limit the use of these pulsars for decade-long gravitational-wave detection efforts. For our most precisely timed pulsars, intrinsic instabilities of the pulsars or the observing system are shown to contribute to timing irregularities on a five-year timescale below the 100 ns level. Based on those results, realistic sensitivity curves for planned and ongoing timing array efforts are determined. We conclude that prospects for detection of a gravitational-wave background through pulsar timing array efforts within five years to a decade are good.

**Key words:** Pulsars – Gravitational Waves

## 1 INTRODUCTION

The rotational behaviour of pulsars has long been known to be predictable, especially in the case of millisecond pulsars (MSPs). Current models suggest that such pulsars have been spun up by accretion from their binary companion star to periods of several milliseconds, making them spin much faster than the more numerous younger pulsars, which typically have periods of about a second. The rotational stability of MSPs is generally 3–4 orders of magnitude better than that of normal pulsars and on timescales of several years, it has been shown that some MSPs have a timing stability comparable to the most precise atomic clocks (Matsakis et al. 1997). This timing stability is most clearly quantified through the technique of pulsar timing, which compares arrival times of pulses to a model describing the pulsar, its binary orbit and the

interstellar medium (ISM) between the pulsar and Earth (as detailed by Edwards et al. 2006). This technique has enabled determination of physical parameters at outstanding levels of precision, such as the orbital characteristics of binary star systems (e.g. van Straten et al. 2001), the masses of pulsars and their companions (e.g. Jacoby et al. 2005; Nice 2006) and the turbulent character of the ISM (e.g. You et al. 2007). The strong gravitational fields of pulsars in binary systems have also enabled stringent tests of general relativity (GR) and alternative theories of gravity, as described by, e.g., Kramer et al. (2006) and Bhat et al. (2008). Finally, pulsars have provided the first evidence that gravitational waves (GWs) exist at levels predicted by GR (Taylor & Weisberg 1982) and have placed the strongest limit yet on the existence of a background of GWs in the Galaxy (Jenet et al. 2006).

Sazhin (1978) was the first to investigate the potential effect of GWs on the times-of-arrival (TOAs) of pulsar pulses and to conclude that direct detection of GWs could be possible through pulsar timing. Subsequent analyses and theoretical predictions for

\*E-mail: Joris.Verbiest@mail.wvu.edu.

astronomical sources of GWs have determined that a stochastic gravitational-wave background (GWB) from binary black holes in the cores of galaxies is the most likely signal to be detectable. As summarised in Jenet et al. (2006), the energy density of such a GWB per unit logarithmic frequency interval can be expressed as:

$$\Omega_{\text{gw}}(f) = \frac{2}{3} \frac{\pi^2}{H_0^2} A^2 \frac{f^{2\alpha+2}}{f_{\text{ref}}^{2\alpha}}, \quad (1)$$

where  $H_0 = 100h \text{ km s}^{-1} \text{ Mpc}^{-1}$  is the Hubble constant,  $f$  is the GW frequency,  $f_{\text{ref}} = (1 \text{ yr})^{-1}$ ,  $A$  is the dimensionless amplitude of the GWB and  $\alpha$  is the spectral index of the GWB. The one-sided power spectrum of the effect of such a GWB on pulsar timing residuals is given by:

$$P(f) = \frac{1}{12\pi^2 f^3} h_c(f)^2, \quad (2)$$

where  $h_c$  is the characteristic strain spectrum, defined as:

$$h_c(f) = A \left( \frac{f}{f_{\text{ref}}} \right)^\alpha. \quad (3)$$

Jenet et al. (2006) also summarized the characteristics and expected ranges for various GWBs of interest. Most importantly, for a GWB created by supermassive black-hole mergers,  $\alpha = -2/3$  and  $A$  is predicted to be between  $10^{-15}$  and  $10^{-14}$  (Jaffe & Backer 2003; Wyithe & Loeb 2003). Sesana et al. (2008) expanded upon these analyses and showed that the actual GWB spectrum strongly depends on the merger history, with a variety of spectral indices possible. They concluded, however, that  $\alpha = -2/3$  was a reasonable approximation for practical purposes. For a background of GWs that were formed in the early Universe,  $\alpha \approx -1$  and the amplitude range predicted by Grishchuk (2005) is  $A = 10^{-17} - 10^{-15}$ , but standard models (e.g. Boyle & Buonanno 2008) predict much lower amplitudes. A third GWB that may be detected by PTAs, is formed by cosmic strings (Damour & Vilenkin 2005; Caldwell et al. 1996), with predicted amplitudes between  $10^{-16} - 10^{-14}$  and  $\alpha = -7/6$  (Maggiore 2000).

Hellings & Downs (1983) first investigated the correlations that arise between timing data of different pulsars due to the presence of a stochastic and isotropic GWB in the Galaxy. They demonstrated that the GWs cause a quadrupolar correlation between the timing residuals of different pulsars. Romani (1989) and Foster & Backer (1990) expanded this analysis and introduced the concept of a pulsar timing array (PTA), in which an ensemble of pulsars is timed and their residuals correlated with each other. The PTA concept uses the quadrupolar correlation signature first derived by Hellings & Downs (1983) to separate the effect of a GW from all other contributions to the residuals, such as intrinsic pulsar timing irregularities, clock errors, ISM effects and Solar System ephemeris errors. Alternatively, the correlation signature for non-Einsteinian GWs (as recently derived by Lee et al. 2008) could be used.

The PTA concept was more rigorously explored by Jenet et al. (2005) who first determined the sensitivity of PTA experiments to backgrounds of GWs (Equation (12) of Jenet et al. 2005). Their analysis showed that the sensitivity of a PTA depends on four main parameters: the number of pulsars, the data span ( $T$ ), the root-mean-square of the timing residuals (simply ‘rms’ or  $\sigma$  henceforth) and the number of observations in each of the pulsar timing data sets ( $N_{\text{TOA}}$ ). They further determined that, for a PTA consisting of weekly observations of 20 MSPs, all with a timing rms of 100 ns, a five-year observational campaign would be required to make a

$\sim 3\sigma$  detection of a GWB with  $\alpha = -2/3$  and  $A = 10^{-15}$ . It follows from Equation (12) of Jenet et al. (2005) that the lowest amplitude of a GWB from supermassive black-hole mergers to which a PTA is sensitive, scales as:

$$A_{\text{min,GWB}} \propto \frac{\sigma}{T^{5/3} \sqrt{N_{\text{TOA}}}} \quad (4)$$

Depending on the achievable rms residual of MSPs, an alternative PTA could therefore achieve the same results through timing of 20 MSPs on a biweekly basis for ten years with an rms of close to 300 ns. This raises two questions related to the potential of PTAs to detect a GWB. First, down to which precision can MSPs be timed ( $\sigma_{\text{min}}$ ) and second, can a low residual rms be maintained over long campaigns (i.e. does  $\sigma/T^{5/3}$  decrease with time)? In the context of this second question, we will henceforth use the term ‘‘timing stability’’ when referring to the potential of an MSP timing data set to maintain a constant, preferably low rms residual at all timescales up to the timespan of a PTA project, which is typically envisaged to be five years or longer.

It has been shown for a few pulsars that timing with a residual rms of a few hundred nanoseconds is possible for campaigns lasting a few years. Specifically, Hotan et al. (2006) presented a timing rms of 200 ns over two years of timing on PSRs J1713+0747 and J1939+2134 (PSR B1937+21) and 300 ns over two years of timing on PSR J1909–3744; Splaver et al. (2005) reported an rms of 180 ns on six years of timing PSR J1713+0747 and Verbiest et al. (2008) timed PSR J0437–4715 at 200 ns over ten years. Similar results for PSRs J0437–4715 and J1939+2134 were obtained by Hobbs et al. (2008) over five years of timing. It has, however, not been demonstrated thus far that MSPs can be timed with an rms residual of  $\leq 100$  ns over five years or more.

The second question - whether a low rms residual can be maintained over ten years or longer, also remains unanswered. Kaspi et al. (1994) detected excess low-frequency noise in PSR J1939+2134; Splaver et al. (2005) presented apparent instabilities in long-term timing of PSR J1713+0747 and Verbiest et al. (2008) noted correlations in the timing residuals of PSR J0437–4715, but apart from these, no long-term timing of MSPs has been presented to date. Given the low rms residual reported on all three sources, it is unclear how strongly the reported non-Gaussian noise would affect the use of these pulsars in a GWB detection effort.

In this article we present the first high-precision long-term timing results for a sample of 20 MSPs. The source selection, observing systems and data analysis methods are described in §2. Our updated timing models and residual plots for all pulsars in our sample are also presented in §2, allowing the reader a fundamental inspection of the reliability of our timing results. In §3, we perform a stability analysis of the timing data, with the dual purpose of identifying low-frequency noise in any of our timing data and of assessing the potential impact of such noise on the use of pulsars in a timing array. In §4 we outline a new way of quantifying different components of the pulsar timing rms. Through this analysis, we separate the levels of receiver noise, noise with a dependency on observing frequency and any temporal instabilities, providing a bound on the residual rms that might be achievable on a five-year timescale. We apply this analysis to three of our most precisely timed pulsars. In §5, we calculate sensitivity curves for ongoing and planned PTAs. These sensitivity curves take into account the inhomogeneous character of a realistic array (i.e. the fact that the rms will differ between pulsars) and assume a bound on residual rms as determined in §4. In §6 we summarise our findings.

## 2 OBSERVATIONS AND DATA REDUCTION

### 2.1 Sample Selection

The data presented in this paper have been collated from two pulsar timing programmes at the Parkes radio telescope. The oldest of these commenced during the Parkes 70 cm MSP survey (Bailes et al. 1994), aiming to characterise properly the astrometric and binary parameters of the MSPs found in the survey. Initial timing results from this campaign were published by Bell et al. (1997) and Toscano et al. (1999). The bright millisecond pulsars PSRs J1713+0747 and B1937+21 (both discovered earlier at Arecibo) were also included in this programme. A few years later, as new discoveries were made in the Swinburne intermediate-latitude survey (Edwards et al. 2001), these pulsars were also added, resulting in a total of 16 MSPs that were regularly timed by 2006. Improved timing solutions for these 16 pulsars were presented by Hotan et al. (2006) and Ord et al. (2006).

Besides the projects described above, the Parkes Pulsar Timing Array (PPTA; Manchester 2008) project commenced more regular timing observations of these pulsars in late 2004, expanding the number of MSPs to 20 (listed in Table 1) and adding regular monitoring at a low observing frequency (685 MHz) to allow correction for variations of the ISM electron density. A detailed analysis of these low frequency observations and ISM effects was recently presented by You et al. (2007) and an analysis of the combined data on PSR J0437–4715 was published by Verbiest et al. (2008). For this pulsar we will use the timing results presented in that publication; for all other pulsars we will present our improved timing models in §2.4.

### 2.2 Observing Systems

Unless otherwise stated, the data presented were obtained at the Parkes 64 m radio telescope, at a wavelength of 20 cm. Two receivers were used: the H-OH receiver and the 20 cm multibeam receiver (Staveley-Smith et al. 1996). Over the last five years, observations at 685 MHz were taken with the 10/50 cm coaxial receiver for all pulsars; however, they were only used directly in the final timing analysis of PSR J0613–0200, whose profile displays a sharp spike at this frequency if coherent dedispersion is applied. For PSRs J1045–4509, J1909–3744 and J1939+2134, the 685 MHz observations were used to model and remove the effects of temporal variations in interstellar dispersion delays and hence are included indirectly in the timing analysis. For all other pulsars any such variations were below the level of our sensitivity.

Three different observing systems were used. Firstly, the Caltech Fast Pulsar Timing Machine (FPTM; Sandhu et al. 1997; Sandhu 2001), between 1994 and November 2001. This is an autocorrelation spectrometer with a total bandwidth of up to 256 MHz. Secondly, the 256 MHz bandwidth analogue filterbank (FB) was used in 2002 and 2003. Finally, the Caltech-Parkes-Swinburne Recorder 2 (CPSR2; Hotan et al. 2006) was used from November 2002 onwards. CPSR2 is a baseband data recorder with two 64 MHz bandwidth observing bands (one usually centred at 1341 MHz, the other at 1405 MHz) and phase-coherent dispersion removal occurring in near real time.

### 2.3 Arrival Time Determination

The processing applied differs for data from different observing systems. The FPTM data were calibrated using a real-time sys-

tem to produce either two or four Stokes parameters which were later combined into Stokes I. The FB data were produced from a search system with no polarimetric calibration possible. This system produced Stokes I profiles after folding 1-bit data. Data from both of these systems were integrated in frequency and time to produce a single profile for each observation. These observations were ~25 minutes in duration. For CPSR2 data, in order to minimise the effects of aliasing and spectral leakage, 12.5% of each edge of the bandpass was removed. To remove the worst radio frequency interference, any frequency channel with power more than  $4\sigma$  in excess of the local median was also removed (“local” was defined as the nearest 21 channels and the standard deviation  $\sigma$  was determined iteratively). CPSR2 also operated a total power monitor on microsecond timescales, which removed most impulsive interference.

The CPSR2 data were next integrated for five minutes and calibrated for differential gain and phase to correct for possible asymmetries in the receiver hardware. If calibrator observations were available (especially in the years directly following the CPSR2 commissioning, observations of a pulsating noise source, needed for polarimetric calibration, were not part of the standard observing schedule). Subsequently the data were integrated for the duration of the observation, which was typically 32 minutes for PSRs J2124–3358, J1939+2134 and J1857+0943 and 64 minutes for all other pulsars. In the case of PSR J1643–1224, the integration time was 32 minutes until December 2005 and 64 minutes from 2006 onwards. Finally, the CPSR2 data were integrated in frequency and the Stokes parameters were combined into total power. CPSR2 data that did not have calibrator observations available were processed identically, except for the calibration step. While for some pulsars (like PSR J0437–4715) these uncalibrated data are provably of inferior quality (see, e.g. van Straten 2006), in our case this is largely outweighed by the improved statistics of the larger number of TOAs and by the extended timing baseline these observations provided. We therefore include both calibrated and uncalibrated observations in our data sets.

Pulse TOAs were determined through cross-correlation of the total intensity profiles thus obtained with pulsar and frequency-dependent template profiles. These template profiles were created through addition of a large number of observations and were phase-aligned for both CPSR2 observing bands. As there were only few high signal-to-noise observations obtained with the FPTM and FB backends for most pulsars, these data were timed against standards created with the CPSR2 backend. This may affect the reliability of their derived TOA errors. For this reason we have evaluated the underestimation of TOA errors for each backend separately, as explained in the next section. While the TOA errors were generally determined through the standard Fourier phase gradient method, the Gaussian interpolation method produced more accurate estimates for pulsars with low signal-to-noise ratios (Hotan et al. 2005) – specifically for PSRs J0613–0200, J2129–5721, J1732–5049, J2124–3358 and J1045–4509. The PSRCHIVE software package (Hotan et al. 2004) was used to perform all of the processing described above.

**Table 1.** Pulsars in our sample. Column 2 gives the reference for the discovery paper, while column 3 provides references to recent or important publications on timing of the sources. For the three pulsars with original B1950 names, these names are given beside the J2000.0 names.

Pulsar name	Discovery	Previous timing solution <sup>a</sup>	Pulse period (ms)	Orbital period (d)	Dispersion measure (cm <sup>-3</sup> pc)
J0437–4715	Johnston et al. (1993)	1, 2	5.8	5.7	2.6
J0613–0200	Lorimer et al. (1995)	3	3.1	1.2	38.8
J0711–6830	Bailes et al. (1997)	3, 4	5.5	–	18.4
J1022+1001	Camilo et al. (1996)	3	16.5	7.8	10.3
J1024–0719	Bailes et al. (1997)	3	5.2	–	6.5
J1045–4509	Bailes et al. (1994)	3	7.5	4.1	58.2
J1600–3053	Ord et al. (2006)	5	3.6	14.3	52.3
J1603–7202	Lorimer et al. (1996)	3	14.8	6.3	38.0
J1643–1224	Lorimer et al. (1995)	4	4.6	147.0	62.4
J1713+0747	Foster et al. (1993)	3, 6	4.6	67.8	16.0
J1730–2304	Lorimer et al. (1995)	4	8.1	–	9.6
J1732–5049	Edwards & Bailes (2001)	7	5.3	5.3	56.8
J1744–1134	Bailes et al. (1997)	3	4.1	–	3.1
B1821–24; J1824–2452	Lyne et al. (1987)	8, 10	3.1	–	120.5
B1855+09; J1857+0943	Segelstein et al. (1986)	3, 9	5.4	12.3	13.3
J1909–3744	Jacoby et al. (2003)	3, 11	2.9	1.5	10.4
B1937+21; J1939+2134	Backer et al. (1982)	3, 9	1.6	–	71.0
J2124–3358	Bailes et al. (1997)	3	4.9	–	4.6
J2129–5721	Lorimer et al. (1996)	3	3.7	6.6	31.9
J2145–0750	Bailes et al. (1994)	3, 12	16.1	6.8	9.0

<sup>a</sup> References: (1) Verbiest et al. (2008); (2) van Straten et al. (2001); (3) Hotan et al. (2006); (4) Toscano et al. (1999); (5) Ord et al. (2006); (6) Splaver et al. (2005); (7) Edwards & Bailes (2001); (8) Hobbs et al. (2004); (9) Kaspi et al. (1994); (10) Cognard & Backer (2004); (11) Jacoby et al. (2005); (12) Löhmer et al. (2004)

**Table 2.** Summary of the timing results, sorted in order of decreasing rms residual. The columns present the pulsar name, the rms timing residual (without prewhitening), the length of the data set and the number of TOAs. For PSRs J1939+2134 and J1857+0943 this table only contains the Parkes data. See §2.4 and §3 for details.

Pulsar name	rms ( $\mu$ s)	T (yr)	N <sub>TOA</sub>
J1909–3744	0.166	5.2	893
J1713+0747	0.198	14.0	392
J0437–4715	0.199	9.9	2847
J1744–1134	0.617	13.2	342
J1939+2134	0.679	12.5	168
J1600–3053	1.12	6.8	477
J0613–0200	1.52	8.2	190
J1824–2452	1.63	2.8	89
J1022+1001	1.63	5.1	260
J2145–0750	1.88	13.8	377
J1643–1224	1.94	14.0	241
J1603–7202	1.98	12.4	212
J2129–5721	2.20	12.5	179
J1730–2304	2.52	14.0	180
J1857+0943	2.92	3.9	106
J1732–5049	3.23	6.8	129
J0711–6830	3.24	14.2	227
J2124–3358	4.01	13.8	416
J1024–0719	4.17	12.1	269
J1045–4509	6.70	14.1	401

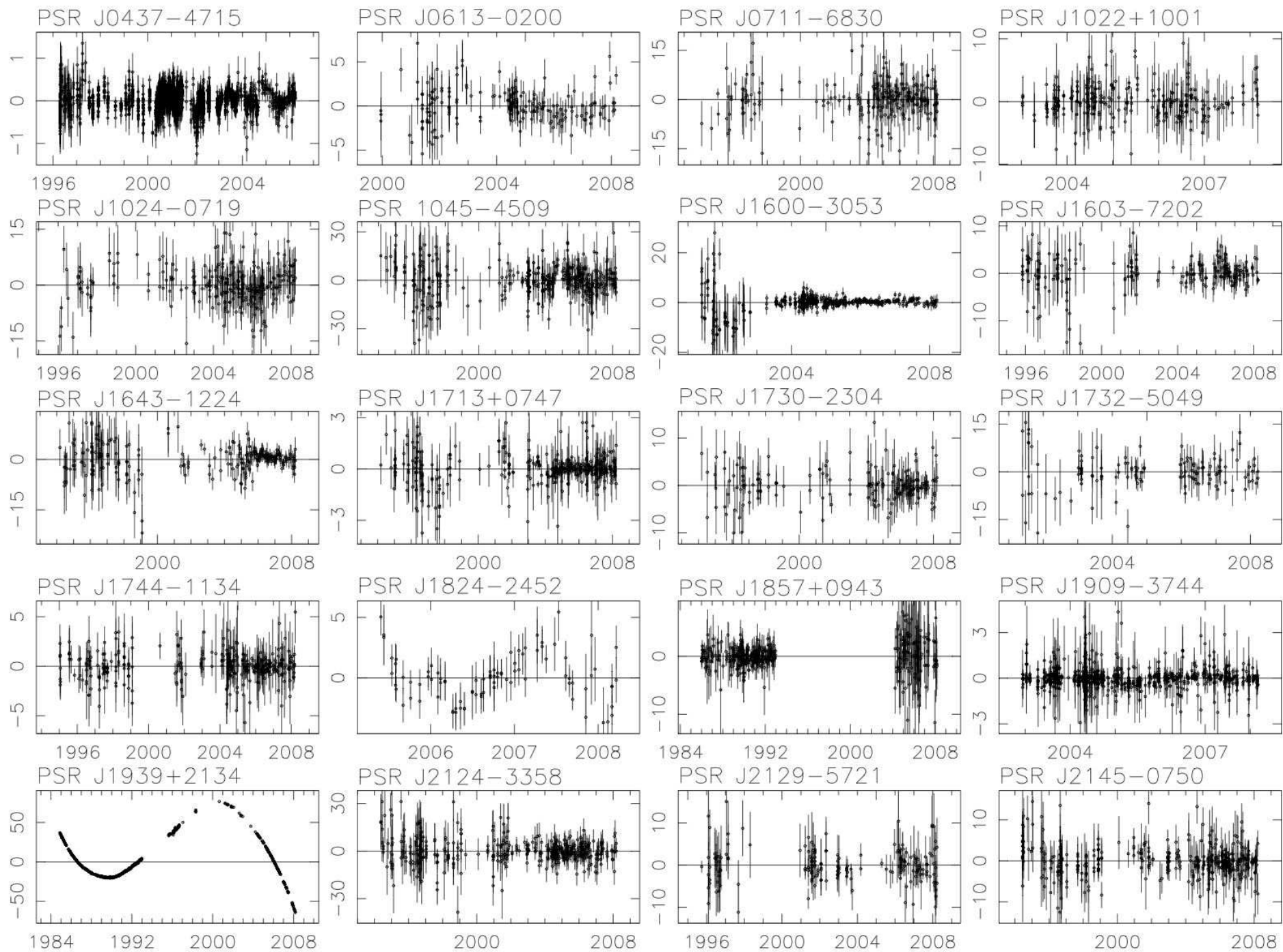


**Figure 1.** Timing residuals of the 20 pulsars in our sample. Scaling on the x-axis is in years and on the y-axis in  $\mu\text{s}$ . For PSRs J1857+0943 and J1939+2134, these plots include the Arecibo data made publically available by Kaspi et al. (1994); all other data are from the Parkes telescope, as described in §2. Sudden changes in white noise levels are due to changes in pulsar backend set-up - see §2 for more details.

**Table 3.** Timing parameters for the single pulsars PSRs J0711–6830, J1024–0719, J1730–2304, J1744–1134, J1824–2452, J1939+2134 and J2124–3358. Numbers in brackets give twice the formal standard deviation in the last digit quoted. Note that these parameters are determined using TEMPO2, which uses the International Celestial Reference System and Barycentric Coordinate Time. As a result this timing model must be modified before being used with an observing system that inputs Tempo format parameters. See Hobbs et al. (2006) for more information.

Fit and data set parameters				
Pulsar name . . . . .	J0711–6830	J1024–0719	J1730–2304	J1744–1134
MJD range . . . . .	49373.6–54546.4	50117.5–54544.6	49421.9–54544.8	49729.1–54546.9
Number of TOAs . . . . .	227	269	180	342
rms timing residual ( $\mu\text{s}$ ) . . . . .	3.24	3.80	2.52	0.617
Reference epoch for P, $\alpha$ , $\delta$ and DM determination . . . . .	49800	53000	53300	53742
Measured Quantities				
Right ascension, $\alpha$ (J2000.0) . . . . .	07:11:54.22579(15)	10:24:38.68846(3)	17:30:21.6611(3)	17:44:29.403209(4)
Declination, $\delta$ (J2000.0) . . . . .	–68:30:47.5989(7)	–07:19:19.1700(10)	–23:04:31.29(8)	–11:34:54.6606(2)
Proper motion in $\alpha$ , $\mu_\alpha \cos \delta$ (mas yr $^{-1}$ ) . . . . .	–15.55(8)	–35.3(2)	20.27(6)	18.804(15)
Proper motion in $\delta$ , $\mu_\delta$ (mas yr $^{-1}$ ) . . . . .	14.23(7)	–48.2(3)	–	–9.40(6)
Annual parallax, $\pi$ (mas) . . . . .	–	–	–	2.4(2)
Dispersion measure, DM (cm $^{-3}$ pc) . . . . .	18.408(4)	6.486(3)	9.617(2)	3.1380(6)
Pulse frequency, $\nu$ (Hz) . . . . .	182.117234869347(4)	193.71568356844(13)	123.110287192301(2)	245.4261197483027(5)
Pulse frequency derivative, $\dot{\nu}$ (10 $^{-16}$ s $^{-2}$ ) . . . . .	–4.94406(15)	–6.95(3)	–3.05906(10)	–5.38188(4)
Prewhitening Terms				
Fundamental wave frequency, $\omega_{\text{pw}}$ (yr $^{-1}$ ) . . . . .	–	0.10368	–	–
Amplitude of wave 1 cosine and sine terms, $A_{\text{cos},1}; A_{\text{sin},1}$ (10 $^{-4}$ s) . . . . .	–	2(13); 4.7(21)	–	–
Fit and data set parameters				
Pulsar name . . . . .	J1824–2452	J1939+2134	J2124–3358	
MJD range . . . . .	53518.8–54544.9	46024.8–54526.9	49489.9–54528.9	
Number of TOAs . . . . .	89	180	416	
rms timing residual ( $\mu\text{s}$ ) . . . . .	0.986	0.354	4.03	
Reference epoch for P, $\alpha$ , $\delta$ and DM determination . . . . .	54219	52601	53174	
Measured Quantities				
Right ascension, $\alpha$ (J2000.0) . . . . .	18:24:32.00796(2)	19:39:38.561297(2)	21:24:43.85347(3)	
Declination, $\delta$ (J2000.0) . . . . .	–24:52:10.824(6)	+21:34:59.12950(4)	–33:58:44.6667(7)	
Proper motion in $\alpha$ , $\mu_\alpha \cos \delta$ (mas yr $^{-1}$ ) . . . . .	–	0.072(2)	–14.12(13)	
Proper motion in $\delta$ , $\mu_\delta$ (mas yr $^{-1}$ ) . . . . .	–9(5)	–0.415(3)	–50.34(25)	
Annual parallax, $\pi$ (mas) . . . . .	–	0.13(13)	3.1(11)	
Dispersion measure, DM (cm $^{-3}$ pc) . . . . .	120.502(2)	71.0227(9)	4.601(3)	
Pulse frequency, $\nu$ (Hz) . . . . .	327.4055946921(6)	641.928233642(12)	202.793893879496(2)	
Pulse frequency derivative, $\dot{\nu}$ (10 $^{-16}$ s $^{-2}$ ) . . . . .	–1736.5(3)	–429.1(6)	–8.4597(2)	
Prewhitening Terms				
Fundamental wave frequency, $\omega_{\text{pw}}$ (yr $^{-1}$ ) . . . . .	0.44734	0.14996	–	
Amplitudes of cosine and sine terms (10 $^{-4}$ s): wave 1: $A_{\text{cos},1}; A_{\text{sin},1}$ . . . . .	–20(6); 2.1(14)	286(41); –413(60)	–	
wave 2: $A_{\text{cos},2}; A_{\text{sin},2}$ . . . . .	–	30(5); 84(12)	–	
wave 3: $A_{\text{cos},3}; A_{\text{sin},3}$ . . . . .	–	–21(3); –5.8(9)	–	
wave 4: $A_{\text{cos},4}; A_{\text{sin},4}$ . . . . .	–	3.7(5); –2.9(5)	–	
wave 5: $A_{\text{cos},5}; A_{\text{sin},5}$ . . . . .	–	0.04(3); 0.68(9)	–	

**Table 4.** Timing parameters for binary PSRs J1022+1001, J1600–3053, J1713+0747, J1857+0943, J1909–3744 and J2145–0750. See caption of Table 3 for more information.

Fit and data set parameters						
Pulsar name	J1022+1001	J1600–3053	J1713+0747	J1857+0943	J1909–3744	J2145–0750
MJD range	52649.7–54528.5	52055.7–54544.6	49421.9–54546.8	46436.7–54526.9	52618.4–54528.8	49517.8–54547.1
Number of TOAs	260	477	392	376	893	377
rms timing residual ( $\mu$ s)	1.63	1.12	0.198	1.14	0.166	1.88
Reference epoch for P, $\alpha$ , $\delta$ and DM determination	53589	53283	54312	50481	53631	53040
Measured Quantities						
Right ascension, $\alpha$ (J2000.0)	10:22:58.003(3)	16:00:51.903798(11)	17:13:49.532628(2)	18:57:36.392909(13)	19:09:47.4366120(8)	21:45:50.46412(3)
Declination, $\delta$ (J2000.0)	+10:01:52.76(13)	–30:53:49.3407(5)	+07:47:37.50165(6)	+09:43:17.2754(3)	–37:44:14.38013(3)	–07:50:18.4399(14)
Proper motion in $\alpha$ , $\mu_\alpha \cos \delta$ (mas yr <sup>–1</sup> )	–17.02(14)	–1.06(9)	4.924(10)	–2.64(3)	–9.510(7)	–9.66(15)
Proper motion in $\delta$ , $\mu_\delta$ (mas yr <sup>–1</sup> )	–	–7.1(3)	–3.85(2)	–5.46(4)	–35.859(19)	–8.9(4)
Annual parallax, $\pi$ (mas)	1.8(6)	0.2(3)	0.94(10)	1.1(4)	0.79(4)	1.6(5)
Dispersion measure, DM (cm <sup>–3</sup> pc)	10.261(2)	52.3262(10)	15.9915(2)	13.300(4)	10.3934(2)	8.9977(14)
Pulse frequency, $\nu$ (Hz)	60.7794479762157(4)	277.9377070984926(17)	218.8118404414362(3)	186.494078620232(2)	339.31568740949071(10)	62.2958878569665(6)
Pulse frequency derivative, $\dot{\nu}$ (10 <sup>–16</sup> s <sup>–2</sup> )	–1.6012(2)	–7.3390(5)	–4.08379(3)	–6.20495(6)	–16.14819(5)	–1.15588(3)
Orbital period, $P_b$ (days)	7.8051302826(4)	14.3484577709(13)	67.825130963(17)	12.32719(4)	1.533449474590(6)	6.83893(2)
Orbital period derivative, $\dot{P}_b$ (10 <sup>–13</sup> )	–	–	41(20)	3(3)	5.5(3)	4(3)
Epoch of periastron passage, $T_0$ (MJD)	53587.3140(6)	53281.191(4)	54303.6328(7)	50476.095(8)	–	53042.431(3)
Projected semi-major axis, $x = a \sin i$ (s)	16.7654074(4)	8.801652(10)	32.3424236(3)	9.230780(5)	1.89799106(7)	10.1641080(3)
$\dot{x}$ (10 <sup>–14</sup> )	1.5(10)	–0.4(4)	–	–	–0.05(4)	–0.3(3)
Longitude of periastron, $\omega_0$ (deg)	97.75(3)	181.85(10)	176.190(4)	276.5(2)	–	200.63(18)
Orbital eccentricity, $e$ (10 <sup>–5</sup> )	9.700(4)	17.369(4)	7.4940(3)	2.170(6)	–	1.930(6)
$\kappa = e \sin \omega_0$ (10 <sup>–8</sup> )	–	–	–	–	–0.4(4)	–
$\eta = e \cos \omega_0$ (10 <sup>–8</sup> )	–	–	–	–	–13(2)	–
Ascending node passage, $T_{asc}$ (MJD)	–	–	–	–	53630.723214894(4)	–
Periastron advance, $\dot{\omega}$ (deg/yr)	–	–	–	–	–	0.06(6)
Sine of inclination angle, $\sin i$	0.73 <sup>1</sup>	0.8(4)	–	0.9990(7)	0.9980(2)	–
Inclination angle, $i$ (deg)	47 <sup>2</sup>	–	78.6(17)	–	–	–
Companion mass, $M_c$ ( $M_\odot$ )	1.05 <sup>3</sup>	0.6(15)	0.20(2)	0.27(3)	0.212(4)	–
Longitude of ascending node, $\Omega$ (deg)	–	–	67(17)	–	–	–



**Table 5.** Timing parameters for binary PSRs J0613–0200, J1045–4509, J1603–7202, J1643–1224, J1732–5049 and J2129–5721. See caption of Table 3 for more information.

Fit and data set parameters						
Pulsar name	J0613–0200	J1045–4509	J1603–7202	J1643–1224	J1732–5049	J2129–5721
MJD range	51526.6–54527.3	49405.5–54544.5	50026.1–54544.7	49421.8–54544.7	52056.8–54544.8	49987.4–54547.1
Number of TOAs	190	401	212	241	129	179
rms timing residual ( $\mu$ s)	1.52	6.70	1.98	1.94	3.23	2.20
Reference epoch for P, $\alpha$ , $\delta$ and DM determination	53114	53050	53024	49524	53300	54000
Measured Quantities						
Right ascension, $\alpha$ (J2000.0)	06:13:43.975142(11)	10:45:50.18951(5)	16:03:35.67980(4)	16:43:38.15544(8)	17:32:47.76686(4)	21:29:22.76533(5)
Declination, $\delta$ (J2000.0)	–02:00:47.1737(4)	–45:09:54.1427(5)	–72:02:32.6985(3)	–12:24:58.735(5)	–50:49:00.1576(11)	–57:21:14.1981(4)
Proper motion in $\alpha$ , $\mu_\alpha \cos \delta$ (mas yr <sup>–1</sup> )	1.84(8)	–6.0(2)	–2.52(6)	5.99(10)	–	9.35(10)
Proper motion in $\delta$ , $\mu_\delta$ (mas yr <sup>–1</sup> )	–10.6(2)	5.3(2)	–7.42(9)	4.1(4)	–9.3(7)	–9.47(10)
Annual parallax, $\pi$ (mas)	0.8(7)	3.3(38)	–	2.2(7)	–	1.9(17)
Dispersion measure, DM (cm <sup>–3</sup> pc)	38.782(4)	58.137(6)	38.060(2)	62.409(2)	56.822(6)	31.853(4)
Pulse frequency, $\nu$ (Hz)	326.600562190182(4)	133.793149594456(2)	67.3765811408911(5)	216.373337551614(7)	188.233512265437(3)	268.359227423608(3)
Pulse frequency derivative, $\dot{\nu}$ (10 <sup>–16</sup> s <sup>–2</sup> )	–10.2308(8)	–3.1613(3)	–0.70952(5)	–8.6438(2)	–5.0338(12)	–15.0179(2)
Orbital period, $P_b$ (days)	1.1985125753(1)	4.0835292547(9)	6.3086296703(7)	147.01739776(5)	5.262997206(13)	6.625493093(1)
Epoch of periastron passage, $T_0$ (MJD)	53113.98(2)	53048.98(2)	–	49577.9689(13)	–	53997.52(3)
Projected semi-major axis, $x = a \sin i$ (s)	1.0914444(3)	3.0151325(10)	6.8806610(4)	25.072614(2)	3.9828705(9)	3.5005674(7)
$\dot{x}$ (10 <sup>–14</sup> )	–	–	1.8(5)	–4.9(5)	–	1.1(6)
Longitude of periastron, $\omega_0$ (deg)	54(6)	242.7(16)	–	321.850(3)	–	196.3(15)
Orbital eccentricity, $e$ (10 <sup>–5</sup> )	0.55(6)	2.37(7)	–	50.578(4)	–	1.21(3)
$\kappa = e \sin \omega_0$ (10 <sup>–6</sup> )	–	–	1.61(14)	–	2.20(5)	–
$\eta = e \cos \omega_0$ (10 <sup>–6</sup> )	–	–	–9.41(13)	–	–8.4(4)	–
Ascending node passage, $T_{asc}$ (MJD)	–	–	53309.3307830(1)	–	51396.366124(2)	–

## 2.4 Timing Results

The TEMPO2 software package (Hobbs et al. 2006) was used to calculate the residuals from the TOAs and initial timing solutions (Table 1). In order to account for the unknown instrumental delays and pulsar-dependent differences in observing setup, arbitrary phase-offsets were introduced between the data from different backends. Where available, data at an observing frequency of 685 MHz were included in an initial fit to inspect visually for the presence of dispersion measure (DM) variations. In the case of PSRs J1045–4509, J1909–3744, J1939+2134 and J0437–4715, such variations were significant and dealt with in the timing software through a method similar to that presented by You et al. (2007). The average DM values presented in Tables 3, 4 and 5 were determined from the 20 cm data exclusively. The uncertainties in these DM values do not take into account possible pulse shape differences between the profiles at these slightly varying frequencies. We updated all the pulsar ephemerides to use International Atomic Time (implemented as TT(TAI) in TEMPO2) and the DE405 Solar System ephemeris (Standish 2004).

In order to correct for any underestimation of TOA uncertainties resulting from (amongst others) the application of CPSR2-based template profiles to the FB and FPTM data (as mentioned in §2.3) and to allow comparison of our timing model parameters to those published elsewhere, the TOA uncertainties were multiplied by error factors (so-called “EFACs”) that are dependent on the pulsar and observing system. Specifically, this part of the analysis was performed as follows. First the timing data from each observing system were prewhitened by fitting harmonically related sine/cosine pairs if required. Next the TOA uncertainties were multiplied by an EFAC value that produced a reduced  $\chi^2$  value of unity for that prewhitened subset of the data. Because of potential non-Gaussian noise in the data, application of these backend-specific EFACs does not necessarily result in a reduced  $\chi^2$  value of unity for the entire, recombined data set. To account for such non-Gaussian noise in the data, a ‘global’ EFAC was applied to the entire data set, making the reduced  $\chi^2$  after prewhitening equal to unity and increasing the parameter uncertainties reported in the timing models appropriately. As mentioned the prewhitening method was based on fitting of sine/cosine pairs to the data, according to the following formula described by Martin (2001) (and replicated in Hobbs et al. 2006):

$$\Delta R = \sum_{k=1}^{n_H} A_{\sin,k} \sin(k\omega_{pw}\Delta t) + A_{\cos,k} \cos(k\omega_{pw}\Delta t)$$

where  $k$  runs over all sine/cosine pairs,  $n_H$  is the total number of harmonically related pairs fitted,  $A_{\cos,k}$  and  $A_{\sin,k}$  are respectively the amplitude of the  $k^{\text{th}}$  cosine and sine waves and  $\omega_{pw}$  is the fundamental frequency derived from:

$$\omega_{pw} = \frac{2\pi}{T(1 + 4/n_H)}$$

with  $T$  the length of the data set. If prewhitening terms were included in the final fit, we provide the values for  $\omega_{pw}$ ,  $A_{\cos,k}$  and  $A_{\sin,k}$  as part of our timing model.

Because the potential non-Gaussian noise present in the data is the subject of our investigations in the remaining sections of this paper, the prewhitening terms as well as the global EFACs were not included in any subsequent analysis. The residuals plotted in Figure 1 and the parameters presented in Table 2 therefore do not include prewhitening terms or global EFACs.

The system-specific EFACs were generally less than two, with

the only major outliers being the CPSR2 data of PSR J1939+2134 with an EFAC of 5.27 and the 32-min CPSR2 integrations (pre-2004 CPSR2 data) of PSR J1643–1224, which have an EFAC of 4.9. In the former case this large EFAC may be caused by incomplete prewhitening, as the non-Gaussian noise is badly modelled by polynomials or sine/cosine pairs. The underestimation of PSR J1643–1224 TOA uncertainties is likely caused by the low signal-to-noise ratio of these observations, which causes the Fourier phase gradient method to underestimate TOA errors (as previously reported by Hotan et al. 2005). We note that the EFAC for the 64 minute integrations is much lower, at 2.5. In deriving the timing models, the global EFAC was at most 1.1 and for more than half of our sources less than 1.05.

The fact that most of our EFAC values are close to unity and show little variation with backend, suggests that the parameter and error estimates are fairly robust. In order to account for the different sensitivity of the backends used and to limit effects of scintillation on our timing, we opt for a weighted analysis. It is therefore important to consider the impact of the TOA errors and applied EFACs on the different parts of this analysis. Given that for most pulsars the EFACs applied to the different backends are nearly equal, the resulting timing models will be little affected by these EFAC values. The reported uncertainties on the timing model parameters will be affected but will be comparable to previous publications, since our analysis method is similar. A full error analysis (as suggested by Verbiest et al. 2008) is needed to provide any more reliable parameter uncertainties. Since the focus of this present paper is on the overall timing stability and implications for pulsar timing array science, we defer such error analysis (and the interpretation of any previously unpublished parameters in our timing models) to a later paper. We have, however, investigated the effect of weighting and EFACs on the timing stability analysis (§3), but have not uncovered any unexpected deviations beyond statistical noise. We therefore conclude that the weighting and applied EFACs do not invalidate our analysis.

A summary of the lengths of the data sets and the achieved rms residual can be found in Table 2, highlighting the superior residual rms of PSRs J1909–3744, J0437–4715 and J1713+0747 when compared to other pulsars. The timing residuals for our data sets are presented in Figure 1 and the timing models are presented in Tables 3, 4 and 5, where  $2\sigma$  errors are given, in accordance with previous practice. We encourage observers to use the improved models when observing. We also note that all but a few of the parameters in our timing models are consistent with those published previously.

## 3 PULSAR TIMING STABILITY

In §1, we demonstrated that one of two vital questions relating to the potential of PTAs to detect a GWB is whether a low residual rms can be maintained over long timespans (a property we refer to as “timing stability”). Effectively, this question breaks down into two parts: to what degree of significance low-frequency noise is present in our pulsar timing data and how any such low-frequency noise can be expected to affect sensitivity to a GWB. In order to answer this question fully, a spectral-analysis-based investigation of pulsar timing residuals that includes identification and modelling of potential non-Gaussian noise sources, would be required. Because of various pulsar timing-specific issues such as clustering of data, large gaps in data sampling and large variations in error-bar size, however, standard spectral analysis methods fail to provide reliable power spectra of pulsar timing data. We therefore use the

alternative approach provided by the  $\sigma_z$  statistic, as described by Matsakis et al. (1997). A brief explanation of this statistic, along with a presentation of the  $\sigma_z$  values of our data is presented in §3.1 and a discussion of these results in terms of PTA-science is provided in §3.2.

### 3.1 $\sigma_z$ Stability Analysis

Originally proposed by Matsakis et al. (1997), the  $\sigma_z$  statistic is defined as:

$$\sigma_z(\tau) = \frac{\tau^2}{2\sqrt{5}} \langle c_3^2 \rangle^{1/2},$$

where  $\langle \rangle$  denotes the average over subsets of the data,  $c_3$  is determined from a fit of the polynomial

$$c_0 + c_1(t - t_0) + c_2(t - t_0)^2 + c_3(t - t_0)^3$$

to the timing residuals for each subset and  $\tau$  is the length of the subsets of the data. In order for the  $\sigma_z$  values to be independent of each other, we use  $\tau = T, T/2, T/4, T/8, \dots$  only. The interpretation of this statistic in terms of power spectra deserves some attention. As presented by Matsakis et al. (1997), a power spectrum with spectral index  $\beta$ :

$$P(\nu) \propto f^\beta$$

would translate into a  $\sigma_z$  curve:

$$\sigma_z(\tau) \propto \tau^\mu,$$

where the spectral indices are related as:

$$\mu = \begin{cases} -\frac{1}{2}(\beta + 3) & \text{if } \beta < 1 \\ -2 & \text{otherwise.} \end{cases} \quad (5)$$

Equation (5) implies that spectra have different slopes in a  $\sigma_z$  graph than in a power spectrum. Along with the  $\sigma_z$  graphs for our data sets, Figure 2 provides some examples of spectra for guidance: lines with a slope of  $-3/2$  (dotted lines in Figure 2) represent spectrally white data ( $\beta = 0$  into Equation (5) gives  $\mu = -3/2$ ) and a GWB with a spectral index  $\alpha = -2/3$  in the gravitational strain spectrum (and therefore a spectral slope  $\beta = -13/3$  in the timing residual spectrum, as follows from equations (2) and (3)) would have a positive slope of  $2/3$  in  $\sigma_z$  (dashed lines).

Comparison of such theoretical slopes to the data is, however, non-trivial since the data are strongly affected by effects from sampling and fitting. As an illustration of such effects, the top-left plot of Figure 2 shows two  $\sigma_z$  curves derived from simulations. The first one is the full line that approximates the  $\sigma_z$  curve for PSR J1713+0747. In this case the  $\sigma_z$  values of 1000 simulations of white noise with the timing rms and sampling of the PSR J1713+0747 data set were averaged. This curve is not perfectly parallel to the theoretical curve with slope  $-3/2$  due to sampling, varying TOA uncertainties and model fitting. Comparison of the white noise simulations with the actual PSR J1713+0747 data indicates that there is not a significant, steep red-noise process affecting the timing residuals for this pulsar. The second simulation in the top-left plot of Figure 2 is the dot-dashed line, which is the average  $\sigma_z$  graph of 2000 simulations of white noise with an artificial GWB and the sampling of the PSR J1939+2134 data set, fitted for pulse period and spindown. This simulated curve does not reach the theoretical slope of  $2/3$  because of flattening off at low frequencies caused by sampling, fitting and leakage resulting from these. This simulation also demonstrates that the PSR J1939+2134 curve is significantly

steeper than a simulated GWB, implying that this pulsar will most likely not be very useful for long-term PTA projects, although its low rms residual on short time spans might make it useful for detection of burst-type sources.

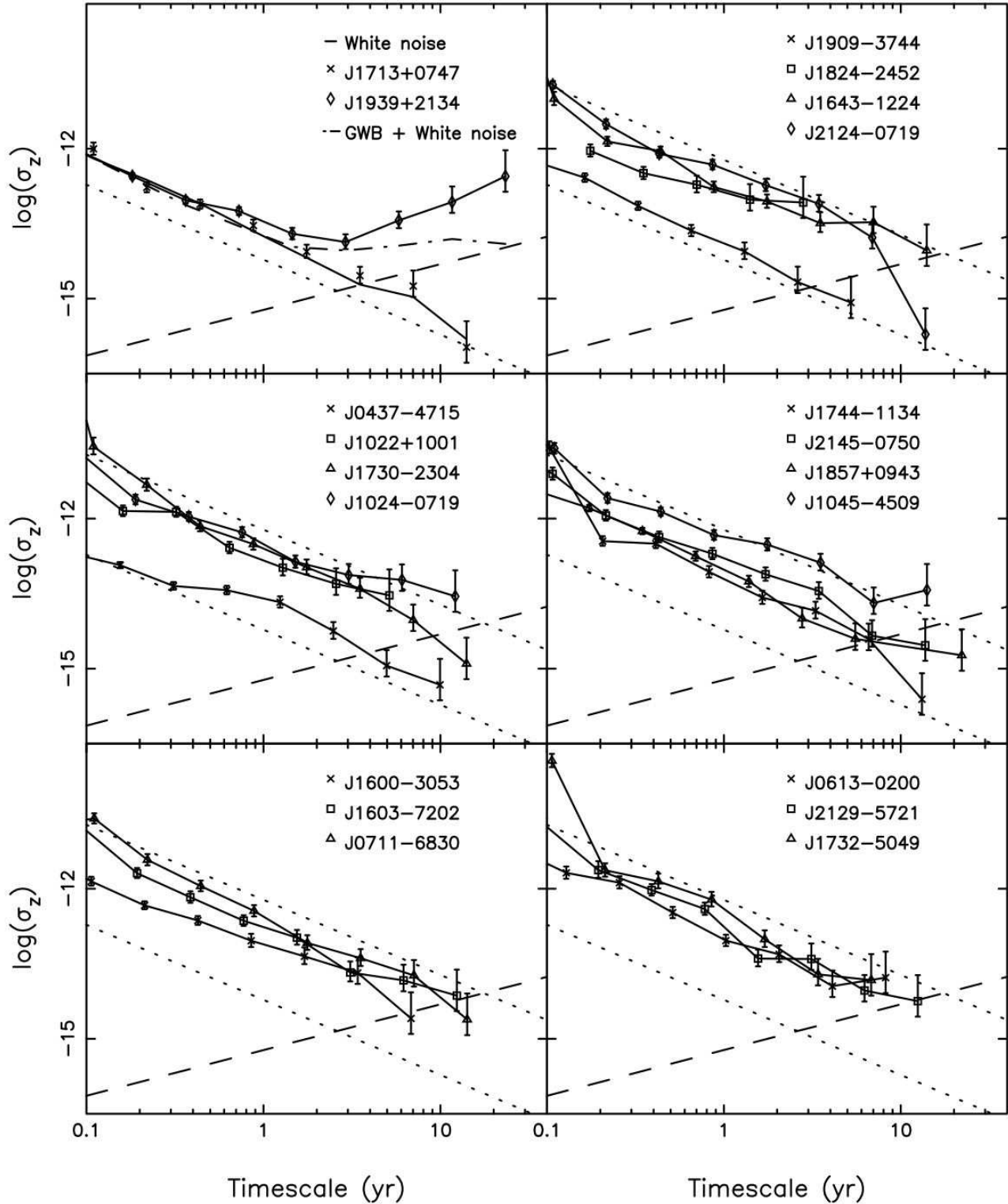


**Figure 2.**  $\sigma_z$  stability parameter for the 20 pulsars in our sample. The dotted slanted lines represent white noise levels of 100 ns (bottom) and 10  $\mu$ s (top); the dashed slanted line shows the steepness introduced to pre-fit residuals by a hypothetical GWB (see §1); pulsars whose curve is steeper than this line (like PSR J1939+2134), can therefore be expected to be of little use to PTA efforts on long timescales. The top left figure further shows the average  $\sigma_z$  values resulting from 1000 simulations of white noise residuals sampled at the times of the PSR J1713+0747 data set and fitted for the PSR J1713+0747 timing model parameters (full line). This demonstrates that the PSR J1713+0747 data do not - within the sensitivity provided by the  $\sigma_z$  statistic - contain a significant, steep red-noise process. The dash-dotted line in the top left figure shows the average of 2000 simulations for white noise combined with a GWB, sampled at the times of the PSR J1939+2134 data set and fitted for pulse period and period derivative. These simulated results provide an example of the combined effect sampling and model fitting can have on the  $\sigma_z$  statistic, even in the case of white noise.

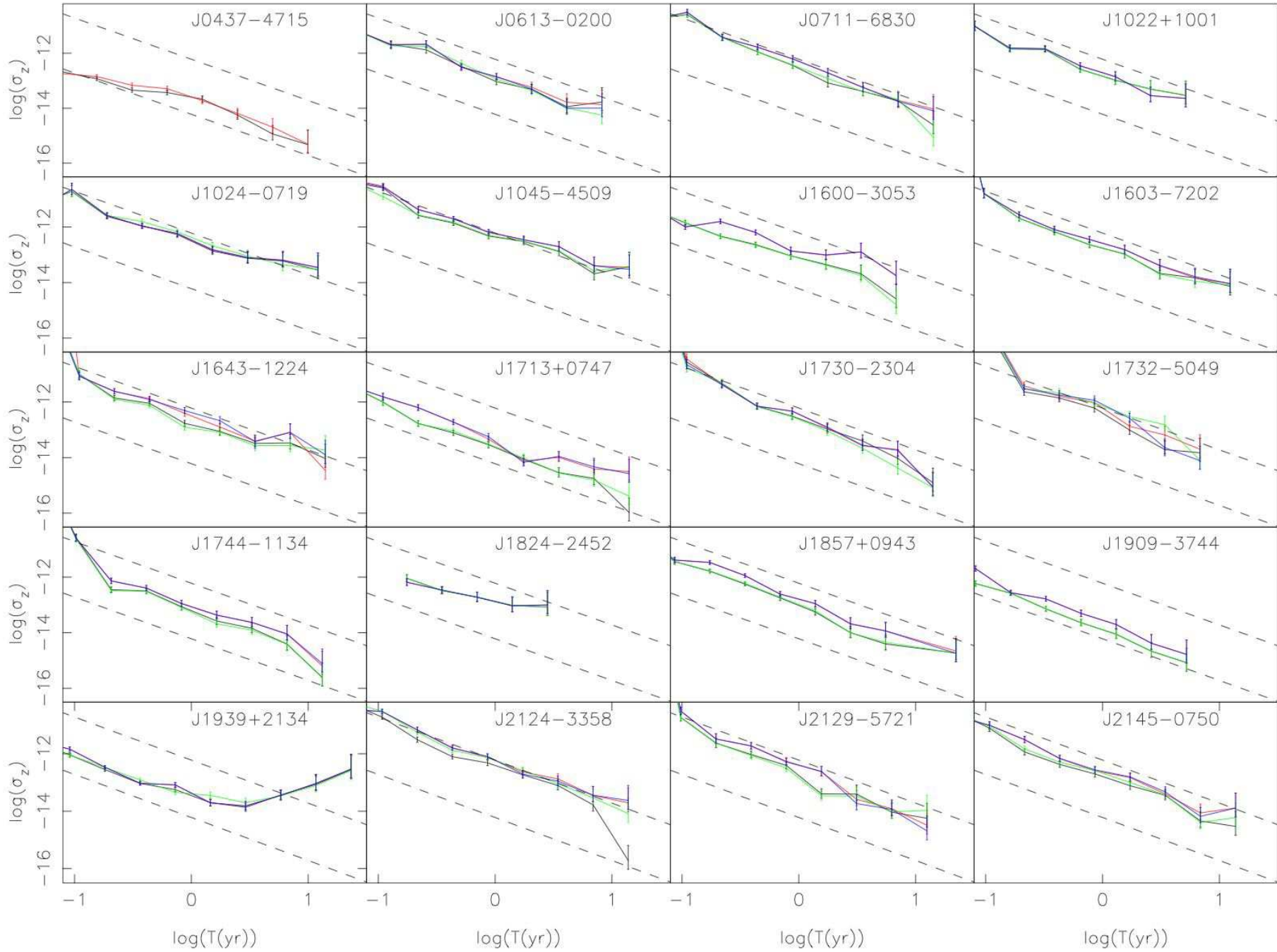


**Figure 3.**  $\sigma_z$  graphs for all pulsars in our sample, showing both weighted (black and green lines) and unweighted (red and blue lines) results, as well as results including EFACs (black and red lines) and excluding EFACs (green and blue lines). The dashed lines represent theoretical white noise at levels of 100 ns and 10  $\mu\text{s}$ . The EFAC values of the PSR J0437-4715 data were lost in processing, so the green and blue curves are missing for that particular pulsar. For all other pulsars all four curves are present, though they do frequently overlap.

The  $\sigma_z$  graphs of our data are shown in Figure 2. A comparison of these curves to those obtained from an unweighted analysis or from an analysis that does not contain the EFAC values described in §2.4, is presented in Figure 3, a colour version of which is available online. This graph demonstrates that use of weighting or EFACs does not affect the data in any statistically significant manner, other than to decrease the effect of the white noise component in case of scintillating pulsars.

Comparison of the PSR J1713+0747 and PSR J1939+2134 data with the simulated curves shown, along with the invariability of the shape of  $\sigma_z$  plots to weighting or application of error factors, shows that the  $\sigma_z$  parameter provides a good first-order discrimination between pulsars that do not exhibit significant, steep red noise (like PSR J1713+0747) and those that do have timing instabilities which could mask a GWB (like PSR J1939+2134).

### 3.2 Timing Stability Conclusions

Figure 2 shows that PSR J1939+2134 has red noise with a level and steepness that will limit its use in GWB-detection efforts that last more than about two years. Four other pulsars (PSRs J0613–0200, J1024–0719, J1045–4509 and J1824–2452) show some indication of similar red noise, but longer timing and lower white-noise levels are needed to determine this with statistical significance. For all the other pulsars we have no evidence that the red noise that may be present in the timing residuals below the white-noise level has a spectral index that prevents GWB detection on timescales of five years to a decade.

We have been unable to detect timing instabilities with an amplitude and spectral slope that could mask a GWB in the timing data of PSRs J1713+0747 and J1744–1134, notwithstanding their long data spans and low timing rms which should make them highly sensitive to any low-frequency noise. Using Equation (4), it can be shown that the data sets of PSRs J1713+0747 and J0437–4715 already meet the requirements for a ten-year long PTA experiment, proving that at least for some pulsars the timing stability and rms residual required to detect a GWB on timescales of ten years or more is achievable. The challenge for such long-term projects will therefore be to find more pulsars like these, or to replicate these results for other existing pulsars, by increasing the sensitivity of observing systems.

It must be noted that the study of irregularities in pulsar timing data (often referred to as “timing noise”) can be much more extensive than presented here. Given our main aim of assessing the impact on PTA science and the absence of clear timing noise in most of our data sets, precise modelling or bounding of timing irregularities as well as a thorough discussion of the potential sources of any observed timing instabilities, has not been included in this analysis.

## 4 ANALYSIS OF RESIDUAL RMS

As an alternative to the long-term PTA detection efforts discussed in the previous section, a shorter-term detection is possible if timing at lower residual rms is achievable. The standard scenario for a (relatively) short-term GWB detection by a PTA requires five years of weekly observations with a timing rms of 100 ns for 20 MSPs (Jenet et al. 2005). Since a residual rms of 100 ns has never been maintained over five years, the possibility that some intrinsic property of MSPs induces instabilities at that level, remains open. In this section, we will address that issue by evaluating how much the

timing rms of some of our most precisely timed pulsars may be reduced.

We separate three different categories of contributions to the pulsar timing residuals:

**Radiometer noise  $\sigma_{\text{Rad}}$ :** The Gaussian noise component that scales with the radiometer equation and which is mainly determined by the shape and signal-to-noise (S/N) ratio of the observed pulse profiles.

**Frequency-systematic effects  $\sigma_\nu$ :** This category of noise contributions contains most effects that produce timing residuals dependent on the observing frequency. This includes interstellar effects such as interstellar scintillation and DM variations.

**Temporal-systematic effects  $\sigma_\tau$ :** This category contains all time-dependent effects such as calibration errors, instabilities in the observing systems, clock errors, errors in the Solar System ephemerides, GWs and intrinsic pulsar timing noise.

As it is impossible to get direct measures of the three contributions listed above, we base our analysis on the following three measurements:

**Total timing rms  $\sigma$ :** This is simply the timing residual rms of the data considered. It contains all three effects:

$$\sigma^2 = \sigma_{\text{Rad}}^2 + \sigma_\nu^2 + \sigma_\tau^2. \quad (6)$$

**Sub-band rms  $\sigma_{\text{sb}}$ :** In §4.2, we will introduce this new measure which is  $1/\sqrt{2}$  times the weighted rms of the offset between the residuals of two simultaneous observing bands with different centre frequencies. Since the observations in the two observing bands are simultaneous, their offset is determined by the radiometer noise and by frequency-systematic effects (as the observing bands are centred at slightly different frequencies). We can therefore write:

$$\sigma_{\text{sb}}^2 = \sigma_{\text{Rad}}^2 + \sigma_\nu^2. \quad (7)$$

**Theoretical radiometer noise  $\sigma_{\text{Rad}}$ :** In §4.1, we will calculate  $\sigma_{\text{Rad}}$  directly from the pulse profiles used in our timing.

Using these three measures and equations (6) and (7), the three contributions to the timing residuals can be isolated, the results of which are described in §4.3.

Our analysis will be based on the CPSR2 data of PSRs J1909–3744, J1713+0747 and J1939+2134. We restrict this analysis to the CPSR2 data because it is of superior quality to the data of older backend systems (see §2.2) and because it consists of the five most densely sampled years of observations. We focus on three of the most precisely timed pulsars in order to obtain the best limits on achievable residual rms. In doing so, we omit PSR J0437–4715 because the advanced calibration schemes used in its analysis (see Verbiest et al. 2008; van Straten 2004, 2006) complicates our efforts and because reported non-Gaussian noise in the timing data of this pulsar (Verbiest et al. 2008) may imply an inferior limit to that derived from PSRs J1909–3744 and J1713+0747. Note that the purpose of this analysis is to uncover the *potential* limit for high-precision timing: it is already known (see e.g. §3) that MSPs have different amounts of time-dependent noise, so the limit we will derive from PSRs J1909–3744 and J1713+0747 does not have to hold for all MSPs. However, it does suggest that other pulsars may achieve similar rms residual and that a PTA-size sample of 20 MSPs at such rms residual may mainly depend on increased sensitivity of current observing systems and new discoveries in ongoing and future surveys.

**Table 6.** Breakdown of weighted timing residuals for three selected pulsars. Given are the total timing rms of the  $\sim 5$  years of CPSR2 data ( $\sigma$ ), the sub-band timing rms ( $\sigma_{\text{sb}}$ ), the radiometer noise ( $\sigma_{\text{Rad}}$ ), the temporal systematic ( $\sigma_{\tau}$ ) and the frequency systematic ( $\sigma_{\nu}$ ) contributions to the timing rms. All values are in ns and apply to 64 min integrations. See §4 for more information.

Pulsar name (1)	$\sigma$ (2)	$\sigma_{\text{sb}}$ (3)	$\sigma_{\text{Rad}}$ (4)	$\sigma_{\tau}$ (5)	$\sigma_{\nu}$ (6)
J1909–3744	166	144	131	83	60
J1713+0747	170	149	105	82	106
J1939+2134	283	124	64	254	106

#### 4.1 Theoretical Estimation of Radiometer Noise, $\sigma_{\text{Rad}}$

The level at which the radiometer noise adds to the timing residuals can be determined based on the pulsar’s observed pulse profile shape and brightness, as described by van Straten (2006). Equation (13) of that publication provides the following measure (notice we only consider the total intensity,  $S_0$ , to allow direct comparison with our timing results):

$$\sigma_{\text{Rad}} = P \times \sqrt{V} = P \times \left( 4\pi^2 \sum_{m=1}^{N_{\text{max}} \leq N/2} \nu_m^2 \frac{S_{0,m}^2}{\zeta_0^2} \right)^{-0.5}, \quad (8)$$

where  $\nu_m$  is the  $m^{\text{th}}$  frequency of the Fourier transform of the pulse profile,  $S_{0,m}^2$  is the total power at that frequency,  $\zeta_0$  is the white noise variance of the profile under consideration,  $N$  is the total number of time bins across the profile and  $N_{\text{max}}$  is the frequency bin where the Fourier transform of the pulse profile reaches the white noise level,  $\zeta_0$ .  $V$  is the expected variance in the phase-offset or residual,  $P$  is the pulse period and  $\sigma_{\text{Rad}}$  is the residual rms predicted for the pulse profile considered.

In order to use Equation (8) on our data, we first integrated all our pulse profiles together, weighted by signal-to-noise ratio, after which Equation (8) was applied to the final profile. Subsequently  $\sigma_{\text{Rad}}$  was renormalised to 64 min integrations through use of the radiometer equation. In order to check this result, we also applied the equation to all individual pulse profiles contained in this analysis and averaged the results in a weighted way - resulting in the same answer, which is given in column four of Table 6. The value for PSR J1909–3744 shows that even at this low residual rms, radiometer noise dominates the timing rms. Applying this method to the other MSPs in our sample, we found that almost all our timing residuals are dominated by radiometer noise. For more than half of our sample of 20 MSPs,  $\sigma_{\text{Rad}}$  is of the order of a microsecond or more. This demonstrates the need for longer integration times, larger bandwidth and/or larger collecting area.

#### 4.2 Estimating Frequency-Dependent Effects

As described in §2.2, the CPSR2 pulsar backend records two adjacent, 64 MHz-wide frequency bands simultaneously. This allows determination of a unique measure of a sub-set of timing irregularities, which we will call the “sub-band rms”,  $\sigma_{\text{sb}}$ :

$$\sigma_{\text{sb}} = \frac{1}{\sqrt{2}} \sqrt{\frac{\sum_i \frac{(r_{i,m} - r_{i,n})^2}{e_{i,mn}^2}}{\sum_i 1/e_{i,mn}^2}}, \quad (9)$$

where the sums run over all observing epochs  $i$ ,  $r_{i,m}$  and  $r_{i,n}$  are the residuals of either observing band (named  $m$  and  $n$  respectively) at epoch  $i$  and  $e_{i,mn} = \sqrt{e_{i,m}^2 + e_{i,n}^2}$  is the average TOA error at epoch  $i$ . Effectively, the sub-band rms is  $1/\sqrt{2}$  times the weighted

rms of the offset between the residuals of the two bands. This implies it contains all contributions to the total rms that are not time-dependent but either statistically white or dependent on the observing frequency, as described earlier. Note, however, that many of these effects have both a temporal and frequency component. Given our sampling, it should therefore be understood that (specifically in the case of DM variations) only part of these effects is contained in  $\sigma_{\nu}$ , while the remaining contributions are contained in  $\sigma_{\tau}$ .

The sub-band rms for the three selected pulsars is presented in column three of Table 6.

#### 4.3 Discussion

Based on equations (6) and (7) and the three measures  $\sigma$ ,  $\sigma_{\text{sb}}$  and  $\sigma_{\text{Rad}}$  determined in the preceding paragraphs, the three contributions to the rms ( $\sigma_{\text{Rad}}$ ,  $\sigma_{\nu}$  and  $\sigma_{\tau}$ ) can now be estimated. Their values are presented in columns 4, 5 and 6 of Table 6. In order to assess the potential for 100 ns timing of these sources over a five-year timescale, we will now discuss the possible means of reducing these three contributions.

The radiometer noise  $\sigma_{\text{Rad}}$  scales for different telescopes or observing systems according to the radiometer equation:

$$\sigma_{\text{Rad}} \propto \frac{T_{\text{sys}}}{A_{\text{eff}} \sqrt{Bt}} \quad (10)$$

where  $B$  is the bandwidth of the observing system used,  $t$  is the integration time,  $A_{\text{eff}} = \eta \frac{\pi D^2}{4}$  is the effective collecting area of the telescope (with  $\eta$  the aperture efficiency and  $D$  the telescope diameter) and  $T_{\text{sys}}$  is the system temperature of the receiver.

The frequency systematic contributions are not as easily scaled for different observing systems, but they can be decreased and research on this front is progressing (You et al. 2007; Hemberger & Stinebring 2008; Walker et al. 2008). Also, by reducing the radiometer noise, any measurements of DM variations will become more precise, which will enhance corrections for these effects and therefore decrease the contribution of  $\sigma_{\nu}$ . We also note that since these effects are frequency dependent, the employment of very large bandwidth receivers or coaxial receiver systems such as the 10/50 cm receiver at the Parkes observatory, may lead to highly precise determination and correction of these effects. Furthermore, increased collecting area and bandwidth may enable future timing observations at higher observational frequencies, which would limit the size of these effects. We therefore suggest that  $\sigma_{\nu}$  does not ultimately limit the achievable rms residual, but may largely be corrected for if current research and technological development progress.

The wide variety of sources that add to the temporal systematic make predictions about its future evolution hard. Sources such as intrinsic pulsar timing noise are (as yet) impossible to mitigate. Errors in the terrestrial clocks or in the Solar System ephemerides

are expected to decrease as better models become available or as timing arrays provide their own improved solutions for these models. Instabilities in the observing system may to some degree be mitigated by improved calibration methods (van Straten 2004, 2006). Simultaneous observations of a single source at multiple observatories may also lead to detection and correction of instrumental instabilities and the time-dependent effect of DM variations may also be mitigated, as explained above.

Following from the above, we stress the fact that all contributions to  $\sigma_\nu$  and  $\sigma_{\text{Rad}}$  may be mitigated, but that certain contributions to  $\sigma_\tau$  cannot be corrected. This implies that this last class of effects will ultimately limit the residual rms that can be reached. We will therefore use the temporal systematic contribution to the rms ( $\sigma_\tau$ , column five in Table 6) as an upper limit on the potential rms residual of the MSPs under investigation. Note that this is a conservative upper limit since significant portions of  $\sigma_\tau$  may be expected to be mitigated. However, without relative quantification of the various contributions to  $\sigma_\tau$ , this limit cannot be reliably decreased.

Given the discussion above, we note that the potential timing residual rms of PSRs J1909–3744 and J1713+0747 is predicted to be below 100 ns on a five-year timescale. This implies that the standard scenario of 100 ns timing over five years is possible provided techniques currently being developed for mitigation of frequency-dependent effects are successful, more sensitive observing systems are used and more bright, stable MSPs like PSRs J1909–3744 and J1713+0747 are found.

## 5 PROSPECTS FOR GRAVITATIONAL WAVE DETECTION

Jenet et al. (2005) derived the expected sensitivity of a PTA to a GWB with given amplitude,  $A$ , both for homogeneous arrays (where all pulsars have comparable timing residuals) and inhomogeneous arrays. They also pointed out the importance of prewhitening<sup>4</sup> the residuals to increase sensitivity at larger GWB amplitudes. In the current section, we will build upon their analysis to provide more realistic predictions for ongoing and future timing arrays. We extend their analysis in three fundamental ways.

Firstly, we use the rms timing residuals presented in Table 2. These results provide an inhomogeneous set of rms's with a realistic spread. We assume the residuals are statistically white and will therefore not change with the timescale of the timing array project. Our analysis in §3 shows that for most pulsars this assumption is reasonable, especially on timescales of order five years.

Secondly, we do not apply exactly the same algorithm as Jenet et al. (2005). In Appendix A, we present a derivation of PTA sensitivity to a GWB in a manner that provides some guidance on analysing the data. We assume that the prewhitening and correlation are handled together by computing cross-spectra and we estimate the amplitude of the GWB directly rather than using the normalised cross correlation function. We assume that the non-GWB noise is white, but can be different for each pulsar. Our results are very close to those of Jenet et al. (2005) and using our method we successfully reproduced the scaling law, Equation (4). The analysis

<sup>4</sup> In this context, prewhitening refers to a technique that flattens the power spectrum of a time series by means of weighting. This flattening optimises the sensitivity of a PTA to steep red spectra such as those introduced by a GWB.

could be easily extended to include non-white noise if a model for the noise were available.

Finally, in order to generalise the results from our Parkes data to telescopes in other parts of the world, we scale the residuals based on realistic parameters for various PTA efforts listed in Table 7. In doing so, we scale  $\sigma_{\text{Rad}}$  (see §4) according to Equation (10). As discussed in §4.3, some improvements in  $\sigma_\nu$  and  $\sigma_\tau$  can be expected in coming years, especially as the radiometer noise is decreased. While quantification of any such improvement is practically impossible, we will apply the same radiometer scaling to  $\sigma_\nu$  as we apply to  $\sigma_{\text{Rad}}$  and assume  $\sigma_\tau$  to be constant at 80 ns for all pulsars at all telescopes. This may provide a slight disadvantage for larger telescopes, but overall we consider this a reasonable yet conservative approach.

### 5.1 Ongoing PTA Projects

We consider five ongoing PTA efforts:

**Current:** Refers to the data presented in this paper, using the longest overlapping time span of the sample: five years. This ignores the fact that the PSR J1824–2452 data set is shorter, but this globular cluster pulsar may not prove useful in a PTA project lasting longer than a few years anyway. We therefore assume that a replacement is found and has identical timing rms over a time span of five years.

**Predicted PPTA:** Assumes the usage of 256 MHz of bandwidth at the Parkes telescope, which implies a four-fold bandwidth increase and therefore a two-fold decrease in timing rms. The PPTA is the only one to be considered for more than five years, mainly in order to demonstrate the large impact a doubling of campaign length can have, but also because several years of high precision timing data with that bandwidth do already exist (Manchester 2008) for all 20 MSPs.

**NANOGrav:** Assumes Arecibo gain for the ten least well-timed pulsars and GBT gain for the ten best-timed pulsars, in order to get a fairly equal rms for all 20 MSPs. (Since we consider  $\sigma_\tau$  an upper limit on the rms residual, the advantage of Arecibo over the GBT is limited for the brightest sources.)

**EPTA:** Assumes monthly observations with five 100 m-class telescopes (Janssen et al. 2008).

**EPTA-LEAP<sup>5</sup>:** Interferometrically combines the five telescopes of the EPTA to form a single, larger one. This decreases the number of observations, but increases the gain.

An important caveat to this analysis is that several of the pulsars under consideration cannot be observed with most Northern telescopes, because of the telescope declination limits. We therefore assume stable MSPs to be discovered in the Northern hemisphere. As mentioned before, we also assume that progress will be made in the mitigation of frequency-dependent ISM and calibration effects. Finally, this analysis is based on the Parkes data presented in this paper and therefore assumes systematic effects to be at most at the level of the Parkes observing system used.

The sensitivity curves presented in Figure 4 seem to justify cautious optimism for GWB detection through PTA experiments on timescales of five to ten years, provided current models of GWBs are correct. While none of the curves in Figure 4 reach the minimum predicted GWB Amplitude of  $10^{-15}$  at a detection-significance level of three, their sensitivity can be expected to in-

<sup>5</sup> Large European Array for Pulsars



crease up to an order of magnitude through extension of the campaigns to a decade-long timescale, as illustrated by the difference between the ‘‘Predicted PPTA’’ and ‘‘Current sensitivity’’ curves. The GWB predictions may, however, change if other effects such as black-hole binary stalling occur. The models do, furthermore, rely on a substantial number of poorly determined input parameters, such as what fraction of galaxy growth happens by merging (Sesana et al. 2009). Since only the merging of galaxies results in binary black holes and hence contributes to the GWB, this mass fraction is crucial for any reliable prediction of GWB strength.

As explained in §4.3, the temporal systematic contribution to the rms,  $\sigma_\tau$ , is a conservative upper limit to the ultimate residual rms. In this analysis of PTA efforts, however, we have used the value of 80 ns as a hard lower limit on the timing rms,  $\sigma$ . This limits the potential for reduction of the rms and explains the equivalence of the NANOGrav and EPTA–LEAP efforts. Finally, the strong dependence on the timescale,  $T$ , of the project underscores the importance of timing stability analysis over much longer time spans and continued observing. While our  $\sigma_z$  analysis on PSR J1713+0747 provides the first evidence for high timing stability over timescales beyond ten years, such timing stability must still be demonstrated for many more MSPs.

## 5.2 Future PTA Projects

With the completion of the Square Kilometre Array (SKA) pathfinders expected in three years time, we consider the potential of the Australian SKA Pathfinder (ASKAP), the South African Karoo Array Telescope (MeerKAT) and the Chinese Five hundred meter Aperture Spherical Telescope (FAST) for PTA programmes. ASKAP is primarily designed for H I surveys and therefore sacrifices point source sensitivity for a wide field of view, whereas MeerKAT’s design is better suited for point source sensitivity over a more limited field of view. FAST is an Arecibo-type single dish with a total diameter of 500 m of which 300 m is illuminated, resulting in a substantially larger sky coverage than is possible with Arecibo. The expected architecture for these telescopes is listed in Table 7 – notice we assume phase-coherent combination of the signals of all ASKAP and MeerKAT dishes, effectively resulting in a single telescope of diameter 107 m for MeerKAT and 76 m for ASKAP.

The resulting sensitivity curves are drawn in Figure 5, along with a hypothetical curve for the most sensitive telescope currently operational, the Arecibo radio telescope. This figure clearly shows the advantage MeerKAT holds over ASKAP for PTA work, in number of dishes, bandwidth and system temperature. The sensitivity of Arecibo is much higher than that of either interferometric prototype and is just inferior to FAST. As for the NANOGrav and EPTA–LEAP projects analysed earlier, the advantage of FAST over Arecibo is strongly limited by the bound of 80 ns we imposed on the achievable rms residual.

Note the usefulness of Arecibo for PTA work is limited by the restricted sky coverage and hence available pulsars. While both MeerKAT and ASKAP can see large parts of the Southern sky, the sky coverage of Arecibo as well as the short transit time make an exclusively Arecibo-based PTA practically impossible; however, its potential as part of a combined effort (Figure 4) or in a global PTA, is undeniable if the level of systematic errors is small compared to the radiometer noise. As for any Northern telescope, the usefulness of FAST will mostly depend on the discovery of good timing MSPs at positive declinations.

## 6 CONCLUSIONS

We have presented the first long-term timing results for the 20 MSPs constituting the Parkes Pulsar Timing Array (PPTA). We have shown that only PSR J1939+2134 has timing instabilities that limit its use for long-term GWB efforts, while the PSR J1713+0747 data already demonstrate the requirements for GWB detection on a timescale of ten to fifteen years are achievable. Overall, the timing stability of the investigated MSPs was found to be encouraging even though potential timing instabilities were detected in four pulsars (in addition to PSR J1939+2134).

It was demonstrated that even on our most precisely timed MSPs, white noise is a dominant contribution, suggesting that our residual rms will be much improved with current wide-bandwidth systems. We placed a conservative upper limit of  $\sim 80$  ns on intrinsic timing instabilities that will ultimately limit the residual rms. We interpreted this result in the context of ongoing and future pulsar timing array projects, demonstrating the realistic potential for GWB detection through pulsar timing within five years to a decade, provided technical and data reduction developments evolve as expected. For PTA efforts in the Northern hemisphere, the discovery of bright and stable MSPs in the Northern sky will be crucial. Given the location of currently known MSPs, the prospects of the MeerKAT SKA pathfinder as a gravitational-wave detector are found to be particularly good.

## APPENDIX A: PTA SENSITIVITY

In this Appendix we derive a simplified formalism for estimating the sensitivity of a pulsar timing array (PTA) to a stochastic and isotropic gravitational-wave background (GWB) of given amplitude,  $A$ . This derivation produces results equivalent to those resulting from equation (14) of Jenet et al. (2005), but is more readily implemented and inherently treats optimal weighting (or prewhitening) of the pulsar power spectra.

The detection statistic is the sample cross-covariance of the residuals of two pulsars  $i$  and  $j$ , separated by an angle  $\theta_{i,j}$ :

$$R(\theta_{i,j}) = \frac{1}{N_s} \sum_{t=0}^T r_i(t) \times r_j(t) \quad (\text{A1})$$

(where  $r_i(t)$  is the residual of pulsar  $i$  at time  $t$ ,  $N_s$  is the number of samples in the cross covariance and  $T$  is the data span). The expected value of  $R(\theta_{i,j})$  is the covariance of the clock error, which is 100% correlated, plus the cross covariance of the GWB,  $\sigma_{\text{GW}}^2 \zeta(\theta_{i,j})$ . The clock error can be included in the fit, but one must also include its variance in the variance of the detection statistic. It is better to estimate the clock error and remove it, which also removes its ‘‘self noise’’. So in subsequent analysis we neglect clock noise and effects of possible Solar System ephemeris errors. We model the pulsar timing residuals as a GWB term and a noise term:  $r(t) = r_{\text{GW}}(t) + r_{\text{N}}(t)$ , with variances  $\sigma_{\text{G}}^2$  and  $\sigma_{\text{N}}^2$ .  $\zeta(\theta_{i,j})$  is the cross-correlation curve predicted by Hellings & Downs (1983), as a function of the angle between the pulsars,  $\theta_{i,j}$ :

$$\zeta(\theta_{i,j}) = \frac{3}{2}x \log x - \frac{x}{4} + \frac{1}{2}$$

in which  $x = (1 - \cos \theta_{i,j})/2$ .

Since the detection significance will be limited by the variance

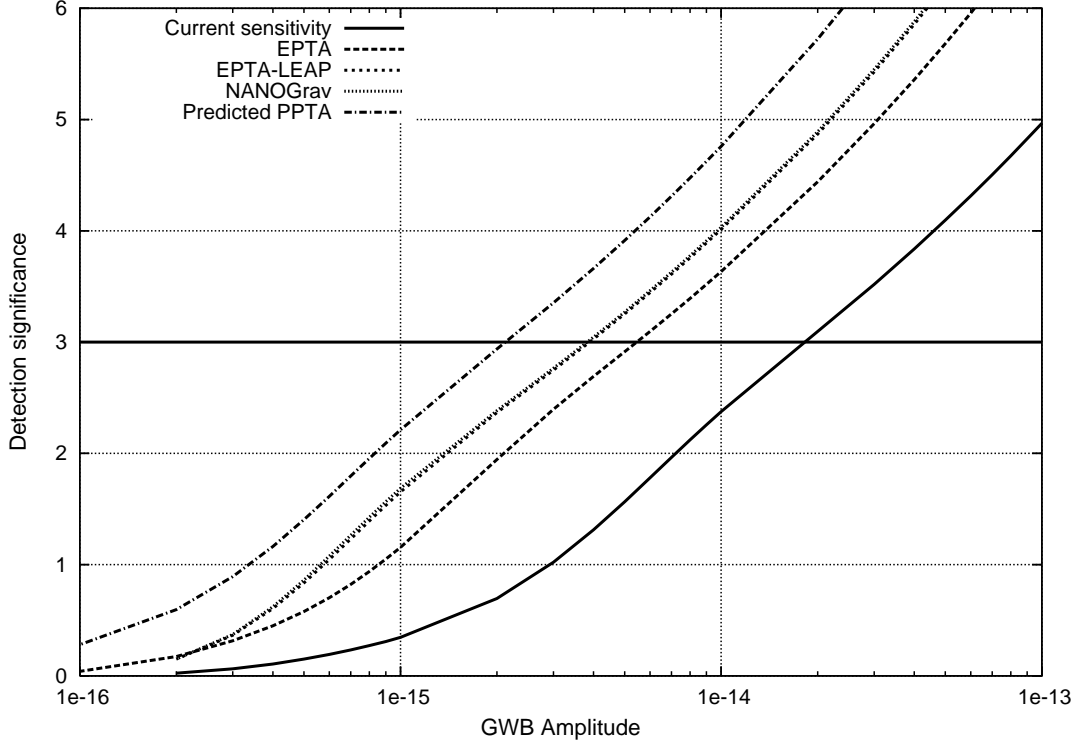


**Figure 4.** Sensitivity curves for different PTA efforts. Note the “NANOGrav” and “EPTA – LEAP” curves are practically coincident. Gravitational waves are predicted to exist in the range  $10^{-15} - 10^{-14}$ . See text and Table 7 for more information.

**Table 7.** Assumed parameters for future and ongoing PTA efforts. Besides the names of the different PTAs, the columns contain the number of telescopes  $N_{\text{Tel}}$ , the observing bandwidth  $B$ , the telescope diameter  $D$ , aperture efficiency  $\eta$ , system temperature  $T_{\text{sys}}$ , observing regularity and the duration of the project,  $T$ .

PTA name	$N_{\text{Tel}}$	$B$ (MHz)	$D$ (m)	$\eta$	$T_{\text{sys}}$ (K)	Observing regularity	$T$ (yrs)
Current	1	64	64	0.6	25	weekly	5
Predicted PPTA	1	256	64	0.6	25	weekly	10
NANOGrav	2	256	305; 100	0.5; 0.7	30; 20	monthly	5
EPTA	5	128	100	0.7	30	monthly	5
EPTA - LEAP	1 <sup>a</sup>	128	224	0.7	30	monthly	5
Arecibo	1	512	305	0.5	30	two-weekly	5
FAST <sup>b</sup>	1	400	500	0.36	20	two-weekly	5
ASKAP <sup>c</sup>	40	256	12	0.8	50	weekly	5
MeerKAT <sup>d</sup>	80	512	12	0.7	30	weekly	5

<sup>a</sup> Under the LEAP initiative, five 100 m-class telescopes will be combined into an effective 224 m single telescope.

<sup>b</sup> Nan (2006); Jin et al. (2008)

<sup>c</sup> <http://www.atnf.csiro.au/projects/askap/specs.html>

<sup>d</sup> Jonas (2007)

in the sample cross covariance, we consider

$$\begin{aligned} & \text{Var}(R(\theta_{i,j})) \\ &= \text{Var}\left(\sum ((r_{\text{GW},i} + r_{\text{N},i})(r_{\text{GW},j} + r_{\text{N},j})/N_s)\right) \\ &= \sigma_{\text{G},i}^2 \sigma_{\text{G},j}^2 \frac{(1 + \zeta(\theta_{i,j})^2)}{N_s} + \frac{\sigma_{\text{N},i}^2 \sigma_{\text{G},j}^2 + \sigma_{\text{G},i}^2 \sigma_{\text{N},j}^2}{N_s} + \frac{\sigma_{\text{N},i}^2 \sigma_{\text{N},j}^2}{N_s}. \end{aligned} \quad (\text{A2})$$

After prewhitening this becomes (notice our notation  $\sigma_{\text{PW}} = \varrho$ ):

$$\begin{aligned} & \text{Var}(R_{\text{PW}}(\theta_{i,j})) \\ &= \varrho_{\text{G}}^4 \frac{(1 + \zeta(\theta_{i,j})^2)}{N_s} + \varrho_{\text{G}}^2 \frac{(\varrho_{\text{N},i}^2 + \varrho_{\text{N},j}^2)}{N_s} + \frac{\varrho_{\text{N},i}^2 \varrho_{\text{N},j}^2}{N_s}. \end{aligned} \quad (\text{A3})$$

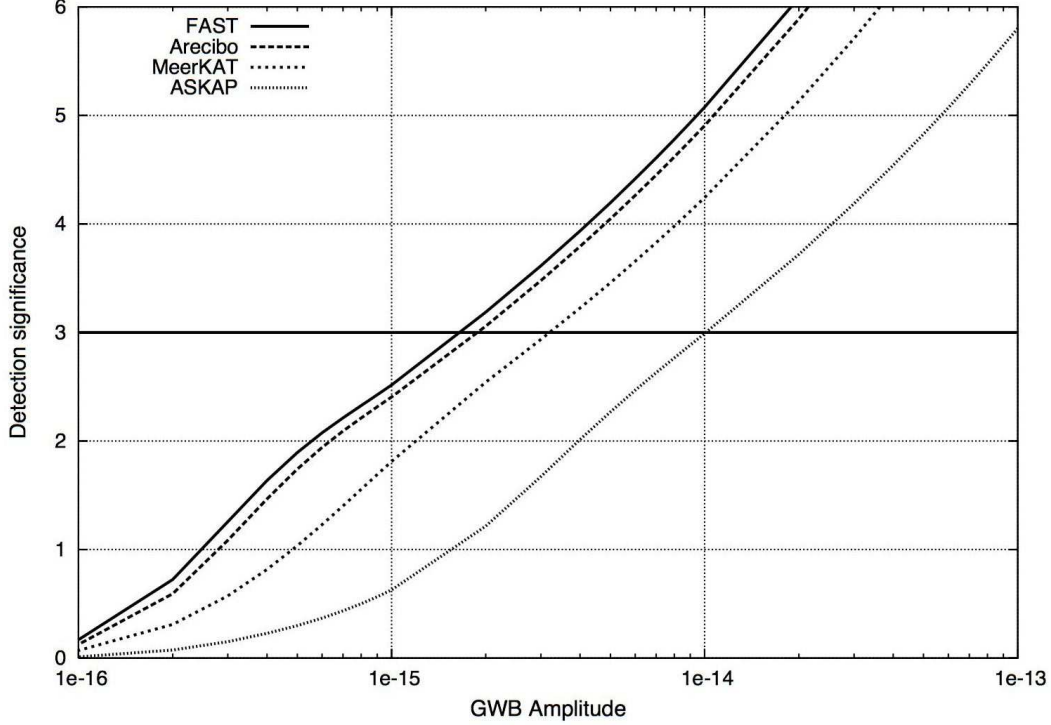


**Figure 5.** Sensitivity curves for the two main SKA pathfinders, Arecibo and FAST. Gravitational waves are predicted to exist in the range  $10^{-15} - 10^{-14}$ . See discussion in §5 and Table 7 for more information.

in which we have used  $\varrho_{G,i}^2 = \varrho_{G,j}^2 = \varrho_G^2$ , which will be proved shortly.

We derive the gravitational-wave power from equations (3) and (2), for a GWB with spectral index  $\alpha = -2/3$ :

$$P_{\text{GWB}}(f) = K(f/f_{\text{ref}})^{-13/3}, \quad (\text{A4})$$

with  $K$  a constant proportional to the amplitude of the GWB and  $f_{\text{ref}} = 1 \text{ yr}^{-1}$ .

Defining the corner frequency,  $f_c$ , as the frequency at which the gravitational wave power equals the noise power, enables us to use equation (A4) to determine the noise power:  $P_{\text{Noise}} = K(f_c/f_{\text{ref}})^{-13/3}$ .

As illustrated by Jenet et al. (2005), the steep spectral index of GWB-induced residuals implies that large gains in sensitivity can be achieved through optimal prewhitening of the data. Assessment of the variance of both the GWB and noise components of the residuals after prewhitening, can most easily be done through integration of the spectral powers, multiplied by the whitening filter,  $W(f)$ , which is a type of Wiener filter, designed to minimize the error in the estimation of  $\sigma_G$  and is of the form:  $W(f) = P_{\text{GWB}}/(P_{\text{GWB}} + P_{\text{Noise}})^2$ . Rescaling the weighting function thus defined, we get:

$$W(f) = C \frac{(f/f_{\text{ref}})^{-13/3}}{(1 + (f/f_c)^{-13/3})^2} \quad (\text{A5})$$

with  $C$  a normalisation constant chosen for convenience to be:

$$C = \left( \sum_f \frac{(f/f_{\text{ref}})^{-26/3}}{(1 + (f/f_c)^{-13/3})^2} \right)^{-1} \quad (\text{A6})$$

The prewhitened variances then become:

$$\begin{aligned} \varrho_G^2 &= \sum_f K(f/f_{\text{ref}})^{-13/3} C \frac{(f/f_{\text{ref}})^{-13/3}}{(1 + (f/f_c)^{-13/3})^2} \\ &= K \end{aligned} \quad (\text{A7})$$

$$\begin{aligned} \varrho_N^2 &= \sum_f K(f_c/f_{\text{ref}})^{-13/3} C \frac{(f/f_{\text{ref}})^{-13/3}}{(1 + (f/f_c)^{-13/3})^2} \\ &= KC \sum_f \frac{(f_c f/f_{\text{ref}})^{-13/3}}{(1 + (f/f_c)^{-13/3})} \end{aligned} \quad (\text{A8})$$

which justifies our choice for  $C$  and shows that, based on our weighting scheme,  $\varrho_{G,i}^2 = \varrho_{G,j}^2 = K$ , as used earlier.

Since the spectra are effectively bandlimited to  $f_c$  after prewhitening, both the GWB and noise will have the same number of degrees of freedom, namely:  $N_{\text{dof}} = 2T_{\text{obs}}f_c - 1$ , where  $T_{\text{obs}}$  is the length of the data span and therefore the inverse of the lowest frequency, implying there are  $T_{\text{obs}}f_c$  independent frequencies measured below  $f_c$ . Since each frequency adds a real and imaginary part, there are twice as many degrees of freedom as there are independent frequency samples; quadratic fitting removes a single degree of freedom from the total. Notice that  $\sqrt{N_{\text{dof},i}N_{\text{dof},j}}$  is the number of independent samples in the cross-covariance spectrum and therefore replaces  $N_s$  in equations (A1) and (A3).

The optimal least-squares estimator for  $K$  (and hence for the amplitude of the GWB), based on a given set  $R_{\text{PW}}(\theta_{i,j})$  with unequal errors, is (from equations (A1) and (A7)):

$$\tilde{K} = \frac{\sum R_{\text{PW}}(\theta_{i,j})\zeta(\theta_{i,j})/\text{Var}(R_{\text{PW},i,j})}{\sum \zeta(\theta_{i,j})^2/\text{Var}(R_{\text{PW},i,j})} \quad (\text{A9})$$

The variance of this estimator is:

$$\text{Var}(\tilde{K}) = \frac{1}{\sum \zeta(\theta_{i,j})^2 / \text{Var}(R_{\text{PW},i,j})} \quad (\text{A10})$$

We can now write the expected signal-to-noise of a given timing array as the square root of the sum over all pulsar pairs of equation (A7) divided by the square root of equation (A10)

$$S = \sqrt{\sum_{i=1}^{N_{\text{PSR}}-1} \sum_{j=i+1}^{N_{\text{PSR}}} \frac{\varrho_G^4 \zeta^2 \sqrt{N_{\text{dof},i} N_{\text{dof},j}}}{\varrho_G^4 (1 + \zeta^2) + \varrho_G^2 (\varrho_{N,i}^2 + \varrho_{N,j}^2) + \varrho_{N,i}^2 \varrho_{N,j}^2}} \quad (\text{A11})$$

Rewriting leads to:

$$S = \sqrt{\sum_{i=1}^{N_{\text{PSR}}-1} \sum_{j=i+1}^{N_{\text{PSR}}} \frac{\zeta^2 \sqrt{N_{\text{dof},i} N_{\text{dof},j}}}{1 + \zeta^2 + (\varrho'_i)^2 + (\varrho'_j)^2 + (\varrho'_i \varrho'_j)^2}} \quad (\text{A12})$$

where  $\varrho'_i = \varrho_{N,i} / \varrho_G$ .

### Acknowledgments.

The Parkes Observatory is part of the Australia Telescope which is funded by the Commonwealth of Australia for operation as a National Facility managed by CSIRO. We thank the staff at Parkes Observatory for technical assistance and dedicated help over many years. We also acknowledge the support of the large number of collaborators and students who have assisted in the acquisition of the data presented in this paper over the last 14 years. JPWV acknowledges financial support provided by the Astronomical Society of Australia (ASA). XPY is supported by the National Natural Science Foundation (NNSF) of China (10803004) and by Natural Science Foundation Project CQ CSTC (2008BB0265).

### REFERENCES

Backer D. C., Kulkarni S. R., Heiles C., Davis M. M., Goss W. M., 1982, *Nature*, 300, 615  
 Bailes M., Harrison P. A., Lorimer D. R., Johnston S., Lyne A. G., Manchester R. N., D'Amico N., Nicastro L., Tauris T. M., Robinson C., 1994, *ApJ*, 425, L41  
 Bailes M., Johnston S., Bell J. F., Lorimer D. R., Stappers B. W., Manchester R. N., Lyne A. G., D'Amico N., Gaensler B. M., 1997, *ApJ*, 481, 386  
 Bell J. F., Bailes M., Manchester R. N., Lyne A. G., Camilo F., Sandhu J. S., 1997, *MNRAS*, 286, 463  
 Bhat N. D. R., Bailes M., Verbiest J. P. W., 2008, *Phys. Rev. D*, 77, 124017  
 Boyle L. A., Buonanno A., 2008, *Phys. Rev. D*, 78, 043531  
 Caldwell R. R., Battye R. A., Shellard E. P. S., 1996, *Phys. Rev. D*, 54, 7146  
 Camilo F., Nice D. J., Shrauner J. A., Taylor J. H., 1996, *ApJ*, 469, 819  
 Cognard I., Backer D. C., 2004, *ApJ*, 612, L125  
 Damour T., Vilenkin A., 2005, *Phys. Rev. D*, 71, 063510  
 Edwards R. T., Bailes M., 2001, *ApJ*, 553, 801  
 Edwards R. T., Bailes M., van Straten W., Britton M. C., 2001, *MNRAS*, 326, 358  
 Edwards R. T., Hobbs G. B., Manchester R. N., 2006, *MNRAS*, 372, 1549  
 Foster R. S., Backer D. C., 1990, *ApJ*, 361, 300  
 Foster R. S., Wolszczan A., Camilo F., 1993, *ApJ*, 410, L91  
 Grishchuk L. P., 2005, *Phys. Uspekhi*, pp 1235–1247  
 Hellings R. W., Downs G. S., 1983, *ApJ*, 265, L39

Hemberger D. A., Stinebring D. R., 2008, *ApJ*, 674, L37  
 Hobbs G., Lyne A. G., Kramer M., Martin C. E., Jordan C., 2004, *MNRAS*, 353, 1311  
 Hobbs G. B., Bailes M., Bhat N. D. R., Burke-Spolaor S., Champion D. J., Coles W., Hotan A., Jenet F., Kedziora-Chudczer L., Khoo J., Lee K. J., Lommen A., Manchester R. N., Reynolds J., Sarkissian J., van Straten W., To S., Verbiest J. P. W., Yardley D., You X. P., 2008, *ArXiv e-prints*  
 Hobbs G. B., Edwards R. T., Manchester R. N., 2006, *MNRAS*, 369, 655  
 Hotan A. W., Bailes M., Ord S. M., 2005, *MNRAS*, 362, 1267  
 Hotan A. W., Bailes M., Ord S. M., 2006, *MNRAS*, 369, 1502  
 Hotan A. W., van Straten W., Manchester R. N., 2004, *PASA*, 21, 302  
 Jacoby B. A., Bailes M., van Kerkwijk M. H., Ord S., Hotan A., Kulkarni S. R., Anderson S. B., 2003, *ApJ*, 599, L99  
 Jacoby B. A., Hotan A., Bailes M., Ord S., Kulkarni S. R., 2005, *ApJ*, 629, L113  
 Jaffe A. H., Backer D. C., 2003, *ApJ*, 583, 616  
 Janssen G. H., Stappers B. W., Kramer M., Purver M., Jessner A., Cognard I., 2008, in Bassa C., Wang Z., Cumming A., Kaspi V. M., eds, 40 Years of Pulsars: Millisecond Pulsars, Magnetars and More Vol. 983 of American Institute of Physics Conference Series, European pulsar timing array. pp 633–635  
 Jenet F. A., Hobbs G. B., Lee K. J., Manchester R. N., 2005, *ApJ*, 625, L123  
 Jenet F. A., Hobbs G. B., van Straten W., Manchester R. N., Bailes M., Verbiest J. P. W., Edwards R. T., Hotan A. W., Sarkissian J. M., 2006, *ApJ*, 653, 1571  
 Jin C. J., Nan R. D., Gan H. Q., 2008, in Jin W. J., Platais I., Perryman M. A. C., eds, IAU Symposium Vol. 248 of IAU Symposium, The fast telescope and its possible contribution to high precision astrometry. pp 178–181  
 Johnston S., Lorimer D. R., Harrison P. A., Bailes M., Lyne A. G., Bell J. F., Kaspi V. M., Manchester R. N., D'Amico N., Nicastro L., Jin S., 1993, *Nature*, 361, 613  
 Jonas J., 2007, in From Planets to Dark Energy: the Modern Radio Universe. October 1-5 2007, The University of Manchester, UK. Published online at SISSA, Proceedings of Science, p.7 Meerkat science and technology  
 Kaspi V. M., Taylor J. H., Ryba M., 1994, *ApJ*, 428, 713  
 Kramer M., Stairs I. H., Manchester R. N., McLaughlin M. A., Lyne A. G., Ferdman R. D., Burgay M., Lorimer D. R., Possenti A., D'Amico N., Sarkissian J. M., Hobbs G. B., Reynolds J. E., Freire P. C. C., Camilo F., 2006, *Science*, 314, 97  
 Lee K. J., Jenet F. A., Price R. H., 2008, *ApJ*, 685, 1304  
 Löhmer O., Kramer M., Driebe T., Jessner A., Mitra D., Lyne A. G., 2004, *A&A*, 426, 631  
 Lorimer D. R., Lyne A. G., Bailes M., Manchester R. N., D'Amico N., Stappers B. W., Johnston S., Camilo F., 1996, *MNRAS*, 283, 1383  
 Lorimer D. R., Nicastro L., Lyne A. G., Bailes M., Manchester R. N., Johnston S., Bell J. F., D'Amico N., Harrison P. A., 1995, *ApJ*, 439, 933  
 Lyne A. G., Brinklow A., Middleditch J., Kulkarni S. R., Backer D. C., Clifton T. R., 1987, *Nature*, 328, 399  
 Maggiore M., 2000, *Phys. Rep.*, 331, 283  
 Manchester R. N., 2008, in Bassa C., Wang Z., Cumming A., Kaspi V. M., eds, 40 Years of Pulsars: Millisecond Pulsars, Magnetars and More Vol. 983 of American Institute of Physics Conference Series, The Parkes Pulsar Timing Array project. pp 584–592

- Martin C. E., 2001, PhD thesis, University of Manchester
- Matsakis D. N., Taylor J. H., Eubanks T. M., 1997, *A&A*, 326, 924
- Nan R., 2006, *Science in China G: Physics and Astronomy*, 49, 129
- Nice D. J., 2006, *Adv. Space Res.*, 38, 2721
- Ord S. M., Jacoby B. A., Hotan A. W., Bailes M., 2006, *MNRAS*, 371, 337
- Romani R. W., 1989, in Ögelman H., van den Heuvel E. P. J., eds, *Timing Neutron Stars Timing a millisecond pulsar array*. Kluwer, Dordrecht, p. 113
- Sandhu J. S., 2001, PhD thesis, California Institute of Technology
- Sandhu J. S., Bailes M., Manchester R. N., Navarro J., Kulkarni S. R., Anderson S. B., 1997, *ApJ*, 478, L95
- Sazhin M. V., 1978, *Sov. Astron.*, 22, 36
- Segelstein D. J., Rawley L. A., Stinebring D. R., Fruchter A. S., Taylor J. H., 1986, *Nature*, 322, 714
- Sesana A., Vecchio A., Colacino C. N., 2008, *MNRAS*, 390, 192
- Sesana, A., Vecchio A., Volonteri M., 2009, *MNRAS*, 394, 2255
- Splaver E. M., Nice D. J., Stairs I. H., Lommen A. N., Backer D. C., 2005, *ApJ*, 620, 405
- Standish E. M., 2004, *A&A*, 417, 1165
- Staveley-Smith L., Wilson W. E., Bird T. S., Disney M. J., Ekers R. D., Freeman K. C., Haynes R. F., Sinclair M. W., Vaile R. A., Webster R. L., Wright A. E., 1996, *PASA*, 13, 243
- Taylor J. H., Weisberg J. M., 1982, *ApJ*, 253, 908
- Toscano M., Sandhu J. S., Bailes M., Manchester R. N., Britton M. C., Kulkarni S. R., Anderson S. B., Stappers B. W., 1999, *MNRAS*, 307, 925
- van Straten W., 2004, *ApJ*, 152, 129
- van Straten W., 2006, *ApJ*, 642, 1004
- van Straten W., Bailes M., Britton M., Kulkarni S. R., Anderson S. B., Manchester R. N., Sarkissian J., 2001, *Nature*, 412, 158
- Verbiest J. P. W., Bailes M., van Straten W., Hobbs G. B., Edwards R. T., Manchester R. N., Bhat N. D. R., Sarkissian J. M., Jacoby B. A., Kulkarni S. R., 2008, *ApJ*, 679, 675
- Walker M. A., Koopmans L. V. E., Stinebring D. R., van Straten W., 2008, *MNRAS*, 388, 1214
- Wyithe J. S. B., Loeb A., 2003, *ApJ*, 590, 691
- You X.-P., Hobbs G., Coles W., Manchester R. N., Edwards R., Bailes M., Sarkissian J., Verbiest J. P. W., van Straten W., Hotan A., Ord S., Jenet F., Bhat N. D. R., Teoh A., 2007, *MNRAS*, 378, 493